

Detecting hidden spatial and spatio-temporal structures in glasses and complex physical systems by multiresolution network clustering

P. Ronhovde¹, S. Chakrabarty¹, D. Hu¹, M. Sahu¹, K. K. Sahu^{1,2}, K. F. Kelton¹, N. A. Mauro¹, and Z. Nussinov^{1,3} ^a

¹ Department of Physics, Washington University in St. Louis, Campus Box 1105, 1 Brookings Drive, St. Louis, MO 63130, USA

² Metal Physics and Technology, ETH, 8093 Zurich, Switzerland

³ Kavli Institute for Theoretical Physics, Santa Barbara, CA93106, USA

October 30, 2018

Abstract. We elaborate on a general method that we recently introduced for characterizing the “natural” structures in complex physical systems via a *multi-scale* network based approach for the data mining of such structures. The approach is based on “community detection” wherein interacting particles are partitioned into “an ideal gas” of optimally decoupled groups of particles. Specifically, we construct a set of network representations (“replicas”) of the physical system based on interatomic potentials and apply a multiscale clustering (“multiresolution community detection”) analysis using information-based correlations among the replicas. Replicas may be (i) different representations of an identical static system or (ii) embody dynamics by when considering replicas to be time separated snapshots of the system (with a tunable time separation) or (iii) encode general correlations when different replicas correspond to different representations of the entire history of the system as it evolves in space-time. Inputs for our method are the inter-particle potentials or experimentally measured two (or higher order) particle correlations. We apply our method to computer simulations of a binary Kob-Andersen Lennard-Jones system in a mixture ratio of $A_{80}B_{20}$, a ternary model system with components “A”, “B”, and “C” in ratios of $A_{88}B_7C_5$ (as in $Al_{88}Y_7Fe_5$), and to atomic coordinates in a $Zr_{80}Pt_{20}$ system as gleaned by reverse Monte Carlo analysis of experimentally determined structure factors. We identify the dominant structures (disjoint or overlapping) and general length scales by analyzing extrema of the information theory measures. We speculate on possible links between (i) physical transitions or crossovers and (ii) changes in structures found by this method as well as phase transitions associated with the computational complexity of the community detection problem. We briefly also consider continuum approaches and discuss the shear penetration depth in elastic media; this length scale increases as the system becomes increasingly rigid.

PACS. 89.75.Fb – 64.60.Cn – 89.65.-s

1 Introduction

This article constitutes a longer companion work to an earlier summary [1] in which the basic notions to be detailed here for complex physical systems were succinctly outlined. We begin by briefly reviewing a special class of complex physical systems that is of great fundamental and technological importance – that of amorphous materials. From a practical standpoint, these materials often have industrial processing and preparation advantages [2, 3] relative to crystalline systems enabling, e.g., greater solubility of pharmaceuticals [4] and many other advantages [2,5]. Below, we list several specific complex amorphous systems. (i) Metallic glasses can be stronger than their respective crystalline structure and exhibit interesting electrical, chemical, and magnetic properties [3]. (ii)

Phosphate glasses are of great use in biomedical applications and chalcogenide glasses are of vital importance in optical recording media such as Blu Ray technology [6]. (iii) Far more recent and exotic challenges involve incommensurate complex electronic structures found in systems such as the high temperature superconductors [7,8]. The understanding of the character of such non-trivial structures is a problem of considerable interest in disparate arenas.

In perfect crystals, the natural system scales are evident by the regular ordering of the lattice. The fundamental unit cells of a crystal typically involve several atoms that are replicated in a simple pattern to span the entire system. There are no intermediate scale structures within the system from the atomic scale of the lattice up to the complete single crystal. Identifying the basic periodic unit cells is vital to the understanding of all crystalline solids.

^a Corresponding author: zohar@wuphys.wustl.edu

This simplicity of structure enables an understanding of crystalline solids in great detail. Early on, the existence of specific unit cell structures were postulated to exist in crystals based on the sharp facets and other macroscopic properties of large crystals.

There are more complex systems in which new structures appear on additional intermediate scales between the atomic-scale and the macro-scale of the system. In recent years, scientific exploration has endeavored to understand a vast array of such complex materials that do not have a simple theoretical starting point.

As alluded to above, some of the best known complex materials are glasses. Liquids that are rapidly cooled (“supercooled”) below their melting temperature avoid crystallization and instead become quenched into an amorphous state. On supercooling, liquids may veer towards *local* low energy structures (that cannot, on their own, be globally replicated to fill space without the inclusion of other structures) before being quenched into an amorphous state. Local low energy structures such as those formed by icosahedral packing are indeed observed in metallic glasses [9,10]. Due to the lack of a simple crystalline reference, the structure of glasses is extremely hard to quantify beyond local scales.

Many theories of glasses rely on the hypothesis of natural structures in the glass [11,12,13,14]. Actually finding such structures in a general way has been more elusive. *How then may we detect and best characterize the most notable structures in amorphous systems?* In the current work, we introduce a general framework to answer this question with specific applications to model glass formers.

The outline of this article is as follows. Initially, we present some background information concerning the pursuit of characterizing structures in glasses and the basic features of our method in Sect. 2. Details of the primary simulated systems are presented in Sect. 3. The community detection and multi-scale community detections methods are explained in Sect. 4. Our multiresolution method is applied to physical models in Sect. 5. We summarize our findings in Sect. 6. Details regarding the applied information measures are given in Appendix A and those concerning our overlapping dynamics procedure in Appendix B; we used this overlapping community detection to augment the community partitions determined by the methods in Sect. 4. Appendix C highlights the simple (yet often overlooked) fact that prepeaks in the structure factor do not constitute a necessary condition for medium range order. In Appendix D, we discuss how we handle “overlapping nodes”- nodes that are common to one or more “communities” within the community detection methods that we employ. The remaining appendices elaborate on additional test cases and various facets of our method. We conclude by discussing structures in space-time and their general properties. We discuss the detection of multi-scale structure in space-time in Appendix R. In Appendix S, we consider continuum approaches and discuss the divergence of a general length

scale- the “shear penetration depth” – as a supercooled liquid becomes quenched into a rigid glass.

2 Background

2.1 Lightning summary of numerous current approaches

Existing work in the pursuit of understanding the glass transition is vast, spanning decades and affecting many fields of science and engineering. Glass formers exhibit several unique common features [15]. Glasses demonstrate short range order (SRO) and medium range order (MRO) structures, but no easily discernible static long range order exists. A striking property of glass formers (especially of the so-called “fragile” glass formers) is that their relaxation times (as measured, by, e.g., their viscosity) can increase by many orders of magnitude over a relatively narrow temperature range. This dramatic slowing down is not associated with the usual distinguishing measures of conventional thermodynamic phase transitions. These systems have rich energy landscapes with an exceptionally high number of metastable states [16,17,18,19,20,21,22].

Given the broad appearance of glass-related states, different frameworks have been explored to work towards a “universal” characterization of the glass transition. Many theoretical approaches, e.g., [15,23,24,25,26,27,14,13] have been developed over the years. The notable theory of random first order transitions (RFOT) investigates mosaics of local configurations [15,23]. RFOT is related [14] to theories of locally preferred structures [14,13,28,11,12]. Other theories seek a similar measures of structure. Amongst many others, these approaches include spin glass type analysis [24], theories of topological defects and kinetic constraints [14,13,29,30,31], and numerous ingenious approaches summarized in excellent reviews, e.g., [19,32,33]. Formally, as demonstrated in [34], a growing static length scale is associated with the diverging relaxation times in supercooled liquids. Some works indeed found indications of increasing correlation lengths (static and those describing dynamic inhomogeneities) as the temperature was lowered [35,36,37,38]. Static correlation lengths were amongst other approaches, notably, examined in terms of (i) “point-to-set” correlations [39,40] as well as (ii) pattern repetition [41]. We will briefly discuss these measures later on.

In metallic glasses, early work to ascertain local structural used a dense random packing model [42]. It was later established that such structures are better represented by an efficient cluster packing (ECP) model [43,44,45]. SRO features were thought to pivot on the existence of local icosahedral structures centered around solute atoms. Various idealized SRO configurations were presented in [46]. Schenk *et al.* experimentally verified icosahedral short range order (ISRO) in undercooled liquids [9]. Kelton *et al.* were the first to experimentally establish a connection between ISRO and the nucleation barrier [10]. Later work further established the importance of ISRO in glasses [47,48,49].

Many structural characterizations are oriented toward static viewpoint of the system, but some dynamical features have also been examined. Analysis of “free volume” (unoccupied space between atoms) fluctuations [45] have been used. Shear stress calculations investigate dynamical processes in glass forming materials [21, 50]. Dynamic heterogeneities involving cooperative motion of structures in a glass have also been studied [51, 52, 53, 54, 55].

Viable characterizations of SRO and MRO structures were advanced for low [56] and high [49] solute concentrations, binary [56, 49], and multicomponent systems [44].

Some methods of characterizing local structures include Voronoi tessellation [57, 31, 56], Honeycutt-Andersen indices [58], and bond orientation ordering parameters [59]. These local measures center on an atom or a given link and, by definition, are restricted from detecting more complex longer range general structures.

Experimental means to directly measure MRO structures are given in [60, 61]. Some potential MRO clusters were examined [22, 56, 49]. Some approaches to understand MRO use pattern matching to idealized MRO structures often constructed as agglomerations of perfectly ordered SRO features.

A very useful experimentally driven approach for ascertaining MRO has been to look for “prepeaks” in X-ray and neutron scattering data [that is, peaks in the structure factor $S(q)$ that appear for wavenumbers q , corresponding to the inverse interatomic distances, which are lower in magnitude than that corresponding to the dominant $S(q)$ peak]. We remark here that while this approach may capture general MRO structures, it is possible to have such structures without structure factor prepeaks (see Appendix C).

2.2 Preliminaries concerning our method

Our unbiased structure characterization method extends *multiresolution* ideas [62] that have generally been reserved for network science applications (analyzing graphs in myriad social and biological networks) to complex materials. Any complex physical system may be expressed as a network composed of nodes that code basic units of interest (e.g., atoms, electrons, etc.). Weighted links may capture the strength of the interactions between the different nodes or experimentally determined correlations (e.g., covariance or partial correlation contributions to the structure factor). After casting the system as a network, we then search for “communities” of nodes (e.g., clusters of atoms) that are more tightly linked to each other (or – in the case of the use of correlation functions as link weights – are more strongly correlated with one another) than to nodes in other clusters [63].

Our multiresolution method employs the notion of “community detection”, see, e.g., [64, 65, 66, 67, 68, 69, 70, 71, 72, 73, 74, 75], to quantitatively identify the “best” scale (or *scales*) for a complex physical system. Our approach *does not* rely on intuition or a knowledge of expected “important” features. Rather, it quantitatively estimates

the best scale(s) through information-theory-based correlations, such as the variation of information (VI) [76] or normalized mutual information (NMI), among different solutions. [In Appendix A, we review these information theory measures.] In essence, different copies of the community detection problem are given to different solvers (“replicas”). If many of these solvers strongly agree regarding certain features of the solution, then these aspects are more likely to be correct. Similarly, a large discrepancy may indicate large fluctuations on a particular scale (or scales). Extrema in NMI or VI among the results of these independent solvers then indicate the best scales for the network.

Multiple extrema can therefore indicate the existence of *multiple relevant length/time scales*. Although in most physical instances there is only a single dominant correlation length, there are many other cases in which more than one length/time scale is present [77].

One distinction between our work and some other established studies of local structures in glasses is that our analysis is not looking strictly at the positional structure. Rather, it evaluates structures in terms of the potential energies (i.e., the internal binding energies of the clusters, see also [22]). Our method can encapsulate weights that represent general statistical (pair of higher order) stress (or other) correlation functions, relative atomic displacements, etc.

Our approach provides a perspective different from the “point-to-set” [78, 79, 34] and other methods [41]. The point-to-set method examines the overlap between configurations in a given volume (a “cavity”) in an equilibrated system and compares those to configurations in the same cavity of the equilibrated system in which the boundary of the cavity was held fixed. Physically, it probes how probable it is to have a particular configuration within a disk or ball of a particular diameter given the boundary conditions. If many small clusters exist inside a sphere of fixed radius, then, a change in the boundary conditions will not significantly alter the bulk cluster distribution within the sphere. Conversely, if the sphere radius is smaller than the natural correlation length, then the number of configurations compatible with the boundary will be small and the overlap will be large. A different but perhaps related approach, that of Ref. [41], examines the distribution of structures inside a given volume to identify the correlation length. The method examines whether the distribution of configurations inside the volume occurs with a random frequency (when the linear scale of the volume is *larger* than the correlation length) or not (when the linear scale of the volume is *smaller* than the correlation length).

Our method does not search for overlap at different scales for a multitude of configurations nor does it examine their frequency. Rather, the pertinent structures are revealed by the information theory extrema between different copies of the entire system. We do not tabulate possible configurations and their occurrence probabilities or examine the system in restricted volumes.

Furthermore, the basic structures that we find may be used as the natural units in a renormalization group type

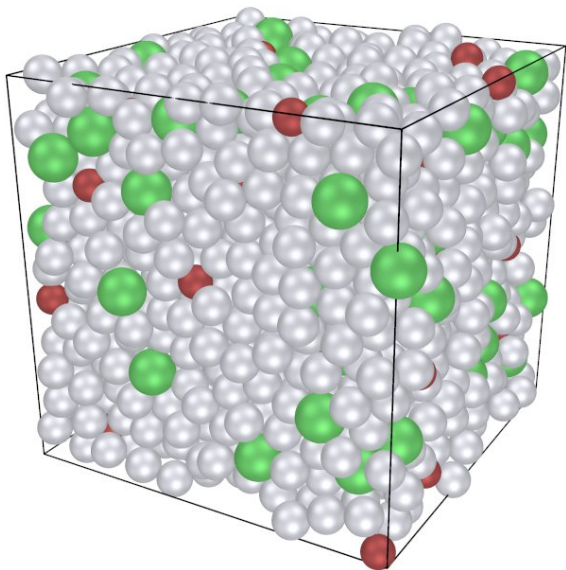


Fig. 1. A depiction of our simulated model glass former with three components “A”, “B”, and “C” with mixture ratios of 88%, 7%, and 5%, respectively. The $N = 1600$ atoms are simulated via IMD [82] in cube of approximately 31 \AA in size with periodic boundary conditions. The identities of the atoms are C (red), A (silver), B (green) in order of increasing diameters.

analysis or coarse grained theories where clusters are replaced by single nodes and an effective energy can be written that entails interactions between the different clusters alone. Finding the basic units is not trivial in amorphous systems such as glasses and numerous disordered systems. In these systems, there is generally no symmetry or any other obvious natural key that may determine how to optimally partition the system on different scales.

3 Simulations of model glasses

We examine a model glass former derived from a three-component AlYFe metallic glass [80] which we designate as “A”, “B”, and “C” in mixture ratios of 88%, 7%, and 5%, respectively. The presence of the different components B and C assists in the formation of a glassy state [81] since few pure compounds manifest a glassy state except under extreme preparation conditions.

3.1 Ternary model glass former

One system that we examine is derived from a three-component AlYFe metallic glass. As depicted in Fig. 1, it is a model glass former with components designated as “A”, “B”, and “C” in mixture ratios of 88%, 7%, and 5%, respectively.

We use classical molecular dynamics (MD) [82] to simulate the system dynamics. For this, we need accurate effective pair potentials that portray the pairwise interactions between the atoms in the system. Our model poten-

	a_0	a_1	a_2	a_3	a_4	a_5
AA	*	*	*	*	*	*
AB	1.92	17.4	6.09	3.05	-4.68	3.48
AC	2.38	8.96	-14.9	3.11	-3.88	4.38
BB	*	*	*	*	*	*
BC	1.88	8.00	-3.42	2.53	-1.25	3.00
CC	*	*	*	*	*	*

Table 1. Fit parameters for Eq. (1) obtained from fitting configuration forces and energies to ab-initio data [83,84]. The units of the parameters are such that given r in \AA , $\phi(r)$ is in eV . (That is, the parameters a_1 , a_4 and a_5 are dimensionless, a_0 is in \AA , a_2 is in $eV \text{\AA}^{a_5}$ and a_3 is in \AA^{-1} .) The same-species (*) data is replaced by a suggested potential derived from generalized pseudo-potential theory [85] (see also Appendix D).

tial energy function is [83]

$$\phi(r) = \left(\frac{a_0}{r}\right)^{a_1} + \frac{a_2}{r^{a_5}} \cos(a_3 r + a_4), \quad (1)$$

where r is the distance between the centers of two atoms. This potential form incorporates a realistic weak long range interaction. Table 1 summarizes the parameter values a_i which depend on the specific types for a pair of interacting atoms, and Fig. 2 shows the respective potential plots.

The interaction parameters $\{a_i\}_{i=1}^5$ were determined [83] by fitting configuration forces and energies to ab-initio data [84]. The same-species model interactions are finally replaced by that suggested by generalized pseudo-potential theory (GPT) [85]. As illustrated in Fig. 1, we simulate $N = 1600$ atoms in a cubic system approximately 31 \AA in size using periodic boundary conditions. This width is approximately twice the size of any suspected MRO structures.

The system is initialized at a temperature of $T = 1500$ K and allowed to equilibrate for a long time using a con-

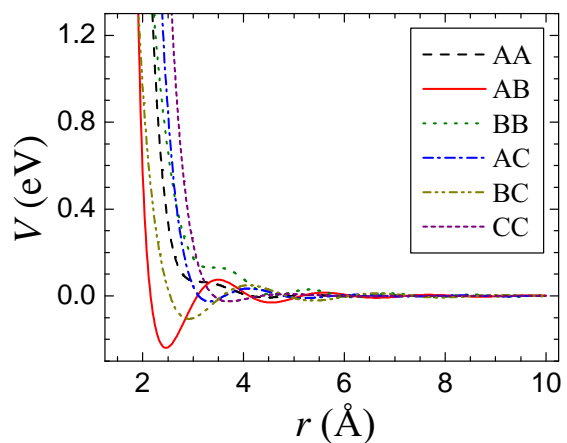


Fig. 2. The pair potentials for our three-component model glass former (see Fig. 1). We indicate the atomic types by “A”, “B”, and “C” which are included with mixture ratios of 88%, 7%, and 5%, respectively. The units are given for a specific candidate atomic realization (AlYFe) discussed in the text. The same-species data uses a suggested potential derived from generalized pseudo-potential theory [85] (see also Appendix D).

stant number of atoms (N), a constant volume (V), and a constant energy (E). That is, we work within the NVE ensemble. After allowing for system equilibration, we save s high temperature configurations separated by a fixed period of simulation time. Prior to cooling, the length scales in the system are changed by 1% to account for the increase in density as a result of cooling since we choose to cool the system in an NVT ensemble to control the temperature. The system is then rapidly quenched to a temperature of $T = 300$ K, and it is allowed to equilibrate (in a mostly frozen state) in an NVE ensemble. We again save s separate low temperature configurations separated by a long period of simulation time.

3.2 Lennard-Jones glass

We additionally test the ubiquitous Lennard-Jones potential using the Kob-Andersen (KA) 80:20 binary liquid [86] which lies in the glass-forming mixture region [87]. The potential is

$$\phi_{\alpha\beta}(r) = 4\epsilon_{\alpha\beta} \left[\left(\frac{\sigma_{\alpha\beta}}{r} \right)^6 - \left(\frac{\sigma_{\alpha\beta}}{r} \right)^{12} \right] \quad (2)$$

where α or β designate one of two atomic types A and B. Specifically, in accord with KA we set the dimensionless units $\epsilon_{AA} = 1.0$, $\epsilon_{AB} = 0.50$, $\epsilon_{BB} = 1.5$, $\sigma_{AA} = 1.0$, $\sigma_{AB} = 0.88$, and $\sigma_{BB} = 0.80$.

As in the ternary glassy system above, we use MD [82] to simulate a LJ system of $N = 2000$ atoms. The system is initialized at a temperature of $T = 5$ (using energy units where the Boltzmann constant $k_B = 1$) and allowed to evolve for a long time. We save s high temperature configurations separated by 1000 time steps. The time step size is $\Delta t = 0.0069$ in LJ time units. Then, the system is rapidly quenched to a temperature of $T = 0.01$ which is well below the glass transition temperature of the KA-LJ system. The system is evolved in this mostly frozen state, and we save s low temperature configurations separated by 1000 steps of simulation time.

4 Multiresolution clustering on amorphous materials

Our idea is to apply, for the first time, multiresolution network analysis methods to ascertain *all* pertinent structures in complex amorphous materials. A key subcomponent of this analysis is the community detection method itself. We first explain these ideas in network analysis and their physical analogs.

4.1 Physical Motivation

In an *ideal decomposition* of a large system into decoupled subsystems (communities), there is no interaction between different communities, and the system is effectively that of an ideal gas of disjoint communities. Stated differently,

in the simplest setting in which the Hamiltonian would be block diagonal, the evolution of nodes (e.g., atoms) in each community would be decoupled from all other nodes in other communities. We next consider a fundamental Newtonian many particle setting. If the total force on a cluster is zero (i.e., if the cluster is strongly decoupled from all others) $\mathbf{F}_{cluster} = 0$ then, the particles in that cluster will drift (on average) with a uniform velocity (the center of mass velocity of that cluster), i.e., $\mathbf{v} \approx \mathbf{const.}$ [88]

In such instances, we may treat each community as a different particle in an ideal gas of non interacting such particles. The general problem is to find (the time dependent) permutation that renders the pair interaction strengths and/or correlations between particles into the best possible block diagonal form (on the time scale chosen). Community detection emulates this for graphs. In the atomic realization that we discuss in this article, this emulates a partition of the system into optimally decoupled clusters such that the system may be viewed as an “*ideal gas*” of *decoupled communities*.

For slow cooling of a liquid which enables crystallization, a first order or critical transition appears in the community detection problem. A similar transition is materialized in many slowly cooled liquids as they crystallize to form nicely ordered solids. By contrast, in an extremely rapid cooling of a liquid, the interactions between the particles are similar to those in spin-glass systems (i.e., the particles are not nicely organized and consequently the inter-particle interactions harbor a large degree of randomness). It is notable that a spin-glass transition appears in the community detection problem for random graphs [89].

4.2 Community detection

In a graph such as that depicted in Fig. 3, nodes correspond to abstracted fundamental elements of the system, and edges represent defined relationships between the nodes. Community detection describes the problem of finding strongly connected groups of nodes. Nodes in different clusters are more weakly connected than the nodes belonging to the same cluster. As alluded to earlier, we apply direct physical analogies where a node corresponds to a single atom. Edges, and their corresponding weights, are directly defined by the associated pair-wise interaction energy (or, in the absence of known interactions, may be set by measured inter-particle correlations). Specifically, we use the interatomic potential energies in Eqs. (1) and (2). This potential model of the network edges is physically appealing in that finding the best partition for the network is akin to minimizing the cluster binding energies of the physical system.

Our Potts model Hamiltonian for community detection is [63]

$$\mathcal{H}(\{\sigma\}) = -\frac{1}{2} \sum_{i \neq j} (A_{ij} - \gamma B_{ij}) \delta(\sigma_i, \sigma_j). \quad (3)$$

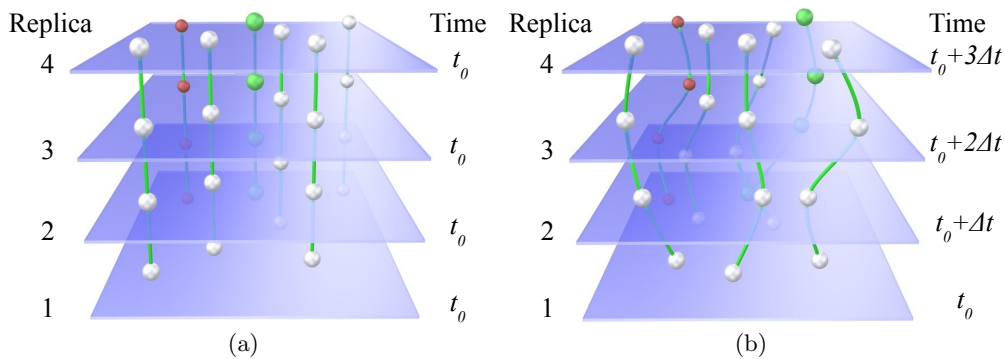


Fig. 4. Panel (a) depicts our replica construction for the physical system at a “static” time t_0 (no time separation between replicas, see Appendix K). For presentation purposes, only a few nodes (atoms) are illustrated. Panel (b) depicts a similar set of replicas separated by a time Δt between successive replicas. In both panels (a) and (b), we generate a model network for each replica using the potential energy between the atoms as the respective edge weights for the network. Independently, within each replica, we then subsequently minimize Eq. (3) at a given value of γ using the algorithm briefly described in Sect. 4.2. Afterwards, we use the information measures in Appendix A to evaluate how strongly the set of replicas agree on the best partition.

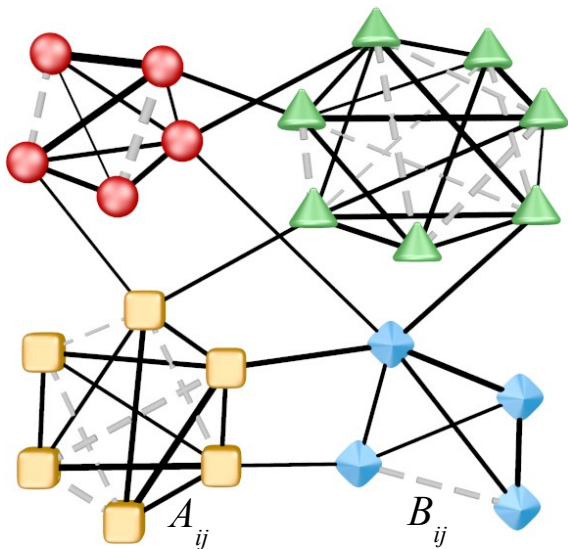


Fig. 3. An arbitrary weighted network with 4 natural communities (strongly connected) depicted as distinct node shapes. The goal in community detection is to identify any such strongly related clusters of nodes based on their defined edge relationships. Solid lines depict weighted links corresponding to complimentary or attractive relationships where $A_{ij} > 0$ and $B_{ij} = 0$ in Eq. (3). Gray dashed lines depict missing, adversarial, or repulsive relationships where $A_{ij} = 0$ and $B_{ij} > 0$ in Eq. (3). In both cases, the relative link weight is indicated by the respective line thicknesses. For presentation purposes, missing intercommunity edges are not depicted. In this paper, we directly relate the edges (attractive and missing/repulsive) to the interaction energy between pairs of atoms which implies that the natural groups would correspond to bound clusters of atoms.

Globally minimizing this Hamiltonian corresponds to identifying strongly connected clusters of nodes. The elements

of the matrices A_{ij} and B_{ij} are the edge weights and are defined as follows: an “attractive” weight has $A_{ij} > 1$ if nodes i and j are connected, $A_{ij} = 0$ if the nodes are not connected, a “repulsive” weight has $B_{ij} \geq 0$ if the nodes are not connected, and $B_{ij} = 0$ if nodes i and j are connected. In this paper, we define model the weights A_{ij} and B_{ij} by pair-wise potential energies (see Sect. 5). In principle, we can generalize the Hamiltonian to include n -body correlations or interactions.

We split the “attractive” (ferromagnetic) and “repulsive” (anti-ferromagnetic) contributions into two separate weighted matrices in order to insert the model weight γ that adjusts the energy trade-off between the two types of interactions. The parameter γ allows us to vary the target scale of the community solution. The spin states σ_i designate the community membership of each node i with a range $1 \leq \sigma_i \leq q$ where q is the number of communities. This number q may be variable [62, 63] (such as in the multi-resolution that we perform in the current work) in order to find the optimal solutions or held fixed. Node i is a member of community k if $\sigma_i = k$. In this Hamiltonian, each spin σ_i interacts *only* with other spins in its *own* community.

Briefly, using Eq. (3) our community detection algorithm rapidly moves nodes between communities based on the current lowest energy assignment until no more moves are possible (see also Appendix B). We then attempt t independent trials and select the lowest energy trial as the best division. [62, 63] [The number of trials serves as our optimization parameter in this greedy algorithm. It effectively allows the algorithm to explore more possible configurations before selecting the best configuration for a given replica. The number of required trials in order to achieve a prescribed accuracy monitors the computational complexity (correlating with the number of local minima in which individual trials may get stuck). Somewhat better optimization could be obtained with a heat

bath solution algorithm [89] at a cost of substantially increased computational effort.] This community detection algorithm partitions the network into communities by assigning a unique cluster membership for each node. Further details are provided in the appendices.

Local features in metallic glasses generally exhibit interconnecting short range structures [56]. In our community detection problem, this feature corresponds to allowing “overlapping” node memberships where atoms can be members of more than one local cluster. We incorporate this effect by assigning a node as a secondary member of every community for which it has a negative binding energy in terms our Potts model in Eq. (3) (see Appendix B).

We can express the general partition function for a community partition with inter-community interactions which may correspond to the surface terms of clusters in Random First Order Transition theory (RFOT). Our parameter γ effectively plays the role of scaling the relation between surface and bulk terms in RFOT. A high value of γ corresponds to large surface effects while a small γ corresponds to dominant bulk effects.

Several strengths of our method are listed below. The analysis is independent of the type of structures that are being analyzed (structured, amorphous solid, and possibly even liquid systems). It is robust to noise in the model network, and it yields very accurate results with a simple and fast greedy algorithm [63]. Because edge assignments are based on relative node positions (through the interaction potential), our method should be robust with respect to translational or rotational motion of solid structures in the system (such as crystal nucleation).

4.3 Multiresolution community detection

Multiresolution methods [90,91,92,62,93] extend the ideas of community detection to identify the “best” division(s) over a range of network scales (“resolutions”). We test s independent realizations of the system (“replicas”) over all relevant network scales by specifying different values of γ in Eq. (3). Networks with a weakly defined structure will result in more diverse solutions among the different replicas. Conversely, strongly defined structures will result in replica solutions that agree more strongly. When replicas represent time-separated configurations, a strong agreement among the replicas corresponds to consistent physical structures over time. The time separation between different snapshots can be tuned to find the corresponding pertinent structures for general time scales. The particular case of vanishing time separation corresponds to different representations of the same static system. See Fig. 4. In the particular case of vanishing time separation, we permute, for identical nodes (atoms), the numbers labeling the nodes within the network; this leads to replicas corresponding to different initial starting points for the algorithm described in Sect. 4.2. [Another possibility now shown in Fig. 4 is that of replicas being different copies of the same system as it evolves in space-time (i.e., a replica not corresponding to a given snapshot of the system at

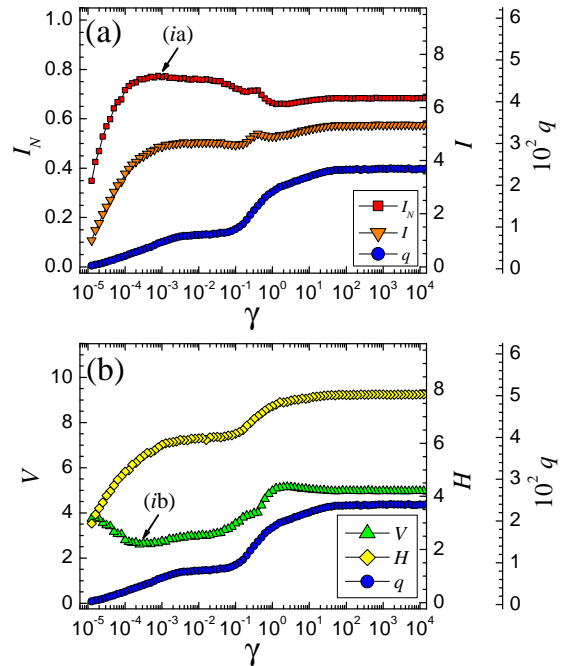


Fig. 6. Panels (a) and (b) show the plots of information measures I_N , V , H , and I and the number of clusters q (right-offset axes) versus the Potts model weight γ in Eq. (3). The ternary model system contains 1600 atoms in a mixture of 88% type A, 7% of type B, and 5% of type C with a simulation temperature of $T = 300$ K which is well below the glass transition for this system. This system shows a strongly correlated set of replica partitions as evidenced by the information extrema at (i) in both panels. A set of sample clusters for the best resolution at $\gamma \simeq 0.001$ is depicted in Fig. 10.

a fixed time but rather monitoring the entire system as it evolves in space-time). This latter possibility will be alluded to in Appendix R.]

Within this framework, we identify the best resolution(s) by analyzing how well the independent replica solutions agree with each other in terms of information content [62]. See Fig. 5 for a schematic involving time separated replicas. Extremal correlated resolution(s) identify the best division(s) of the network. We apply the variation of information (VI) V metric and the normalized mutual information (NMI) I_N measure to evaluate the level of similarity among all pairs of the s replicas (see Appendix A). Extrema correspond to locally stable solutions that remain locally unchanged for variations in the system scale. In the case of very stable system resolutions, local extrema can be replaced by plateaus in these information theory measures that indicate no change in the system solution over an extended range of resolution scales γ (as seen in the networks examined in [62] and, in the appendix of the current work, in some crisp lattice systems analyzed in Appendix O). We can further extract additional qualitative information about the “stability” of network partitions across a range of resolutions by examining the average number of clusters q [90,91,94], mutual information I [90], or the Shannon entropy H [62,94].

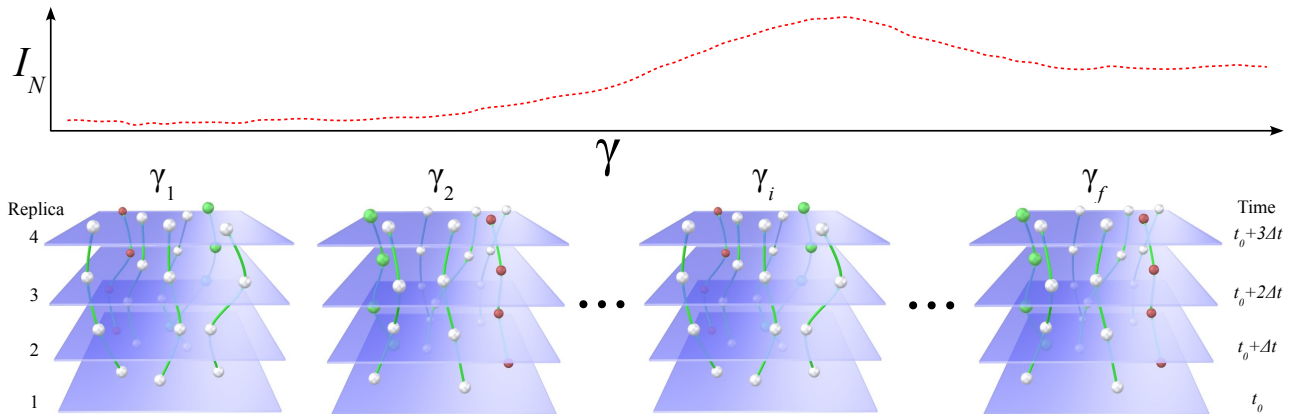


Fig. 5. A depiction of our multiresolution algorithm using the replicas of Fig. 4(b) for a range of resolution parameters γ in Eq. (3). We solve the set of replicas at each γ_i after which we utilize the information measures in Appendix A, such as I_N in the schematic, to measure the level of agreement among the replicas for each tested resolution. The NMI I_N or VI V extrema (or plateaus in some instances) indicate preferred (or more “stable”) resolutions.

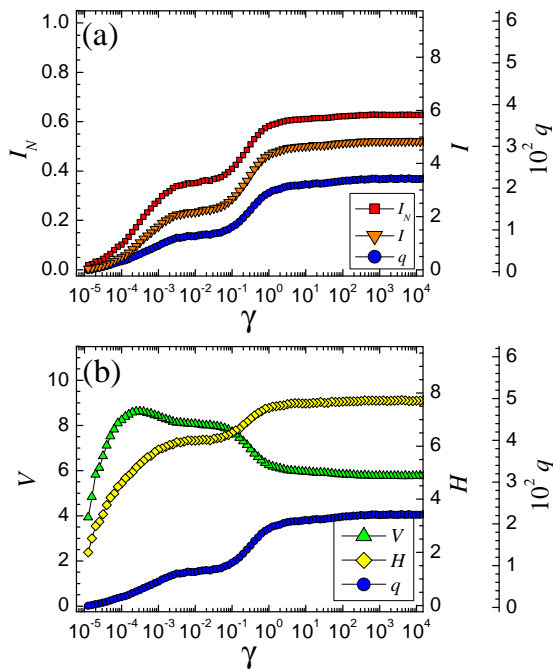


Fig. 7. Panels (a) and (b) show the plots of information measures I_N , V , H , and I and the number of clusters q (right-offset axes) versus the Potts model weight γ in Eq. (3). The ternary model system contains 1600 atoms in a mixture of 88% type A, 7% of type B, and 5% of type C with a simulation temperature of $T = 1500$ K which is well *above* the glass transition for this system. At this temperature, there is no resolution where the replicas are strongly correlated. See Fig. 6 for the corresponding low temperature case where the replicas are much more highly correlated at $\gamma \simeq 0.001$.

4.3.1 Phase diagram of the community detection problem

Apart from trying to find the best possible division of communities in a particular system, we have also looked at the ease at which such a solution can be found. This further indicates when, physically, the system might be analyzed

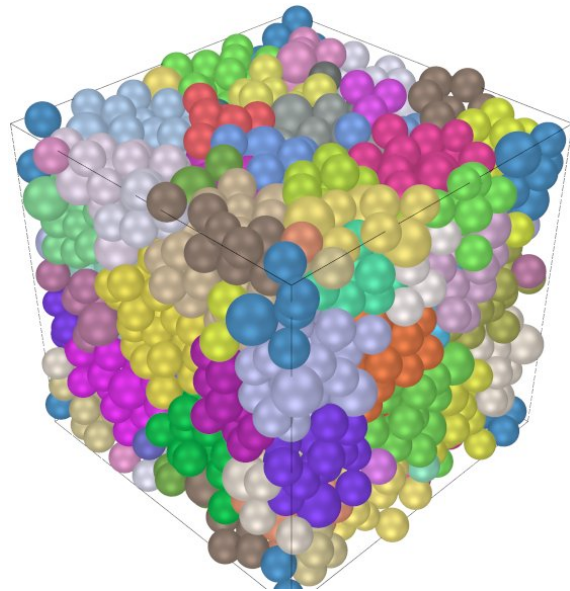


Fig. 8. A depiction of the full *partitioned* system where unique cluster memberships are depicted as distinct colors (best viewed in color). The atomic identities are B, A, C in order of increasing diameters. Overlapping nodes (multiple memberships per node) are added to these communities to determine the best interlocking system clusters.

in terms of nearly decoupled communities and when it cannot. It also enables us, by varying the parameters and temperature to map out when a solution is present or not, to determine whether the solutions found can be trusted and are physically relevant.

When solving the system of Eq. (3) at non-zero temperature for a given network (i.e., for an atomic configuration that is held fixed), entropic effects can, on their own, lead to a transition as the temperature is increased [89]. This transition corresponds to a spin glass type transition for random systems capturing a transition from easy to hard computational problems. These transitions may

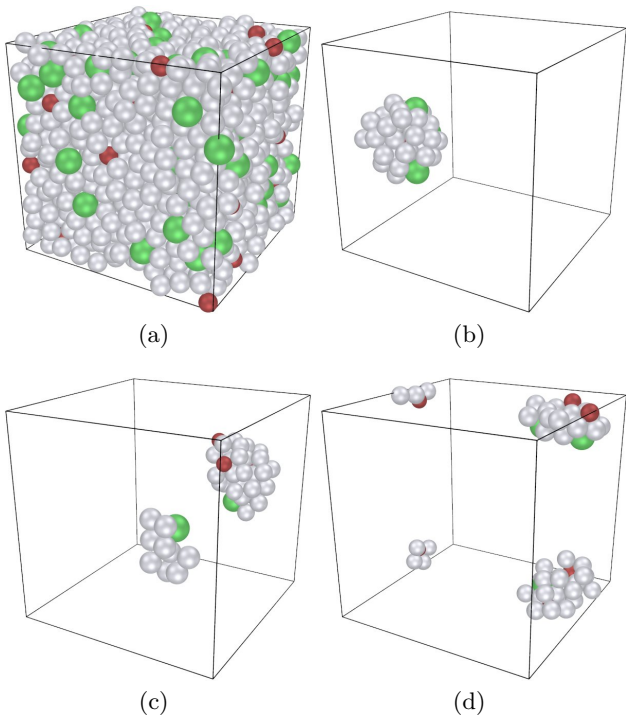


Fig. 9. Panel (a) is the full system cube, and panels (b) – (d) show three sample clusters (one distinct cluster each using periodic boundary conditions) within the simulation box. Note that the algorithm can identify structures beyond immediate short range neighbors.

also be standard equilibrium transitions for sufficiently regular systems – critical for several regular graphs (e.g., the square lattice viewed as a graph analyzed via a Potts model for $q \leq 4$ communities) or first order ($q > 4$ in the example above); for weak disorder, the latter transitions may be rounded off and further display signatures of Griffiths type behavior [101]. We briefly elaborate on this idea below. As illustrated in the examples analyzed in this work, spatially increasing low temperature structures in a supercooled liquid as well as correlation lengths in systems such as the Ising spin systems can be ascertained via our method. In a general decomposition of an interacting system into optimally decoupled groups of particles (“communities”), the partition function is approximated as

$$Z \simeq \sum_{\{\Lambda\}} g(\Lambda) \prod_{c=1}^{q_\Lambda} z_c. \quad (4)$$

Here, z_c is the partition function as computed with the Hamiltonian of the entire system for the particles in community c , $g(\Lambda)$ is the frequency of obtaining a particular set of communities Λ in a decomposition of the entire system into optimally disjoint communities, and q_Λ is the total number of communities in the partition Λ . Thus, physical transitions or crossovers may, in this approximation, be related to transitions (or divergent scales) or crossovers in the communities found in Λ themselves and/or phase

transitions associated with the computational complexity of the community detection problem (as further manifest via the distribution of partitions $g(\Lambda)$) [89]. A decomposition of the type of Eq. (4) is exact for a (standard uniform) q state Potts model ($H = -\frac{1}{2} \sum_{i \neq j} A_{ij} \delta_{\sigma_i, \sigma_j}$ where $A_{ij} = 0, 1$) wherein the interaction energy between spins in different clusters (with each cluster/community given by uniform value of σ_i) is identically zero ($\delta_{\sigma_i, \sigma_j} = 0$).

In Fig. 11, we plot a specific measure [62] of the computational complexity as a function of the density of energetically attractive inter-community links p_{out} and temperature T for a particular random graph. Within the solvable flat region (starting at low p_{out} and T) the system can be effectively decomposed into decoupled elements, i.e., the partition function satisfies Eq. (4) with a well-defined set of partitions $\{\Lambda\}$. This region is separated by ridges of high complexity in which the community detection problem becomes exceedingly hard from the unsolvable region in which no sensible community detection occurs (weak thermal fluctuations aid the system in avoiding metastable states while large thermal fluctuations are detrimental). While the specific phase diagram boundaries were found with the Hamiltonian of our method (discussed next), the phase diagram changes little when other methods are used. In several simple cases the phase boundaries coincide with those of the known cases (e.g., the phase transition of the Ising model on the square lattice when investigated as a network with links representing the strength of the spin exchange).

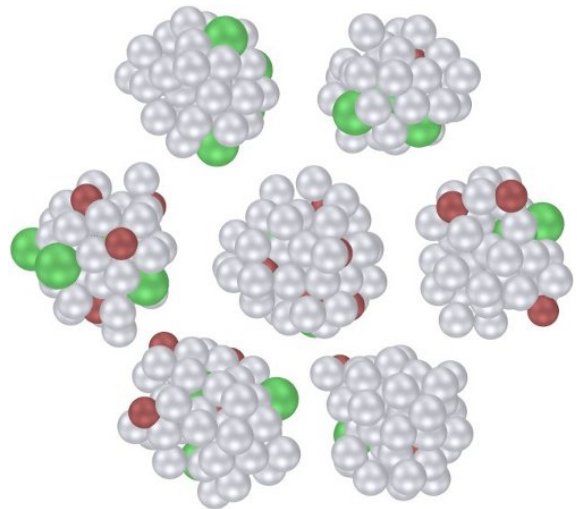


Fig. 10. A depiction of some of the best clusters of the low temperature ($T = 300K$) ternary system at the peak replica correlation at feature (i) in Fig. 6. These clusters include overlapping node membership assignments where each node is required to have an overall negative binding energy to the other nodes in the cluster. The atomic identities are C (red), A (silver), B (green) in order of increasing diameters.

5 Multiresolution application to model glass formers

We assign edges between the nodes (atoms) with the respective weights based on the empirical pair-potentials given by Eqs. (1) and (2). Specifically, we calculate the potential energy ϕ_{ij} between each pair of nodes i and j in the system and then shift each value by a constant ϕ_0 to obtain $\phi'_{ij} = \phi_{ij} + \phi_0$ (assuming that $\phi_{ij} \rightarrow 0$ as the distance between particles i and j tends to infinity ($r \rightarrow \infty$)). The shift $\phi_0 > 0$ is necessary for the community detection algorithm to properly partition the network of atoms since it provides an objective definition of which interatomic spacings are preferable for a well-defined cluster and which are preferred to be excluded from a cluster.

In our particular application here, we calculate the average potential energy of the system and set $\phi_0 = -\phi_{\text{avg}}$. For use in Eq. (3), we define an edge with a weight $A_{ij} = -\phi'_{ij}$ between nodes i and j if $\phi'_{ij} < 0$, and we weight any missing links (or “repulsive edges”) by $B_{ij} = \phi'_{ij}$ if $\phi'_{ij} \geq 0$. We then solve both model systems over a large range of γ using $s = 12$ replicas and $t = 10$ optimization trials per replica.

While $\phi_0 = -\phi_{\text{avg}}$ is an intuitive shift that accomplishes the goal of an objective cluster definition here, it is not an appropriate shift for some problems. For example, using $\phi_0 = -\phi_{\text{avg}}$ turns out to be problematic in some cases for lattice models. In a general setting, we examine a continuum of potential shifts ϕ_0 and monitor extrema in the information theory measures as a function of both γ in Eq. (3) and ϕ_0 .

In addition to the systems tested below, we applied the algorithm to various test cases including square, triangular, and cubic lattice structures. The algorithm is able to correctly identify the natural leading order scales (plaquettes and composites of plaquettes as “cascades” in the information theory correlations). Further testing in-

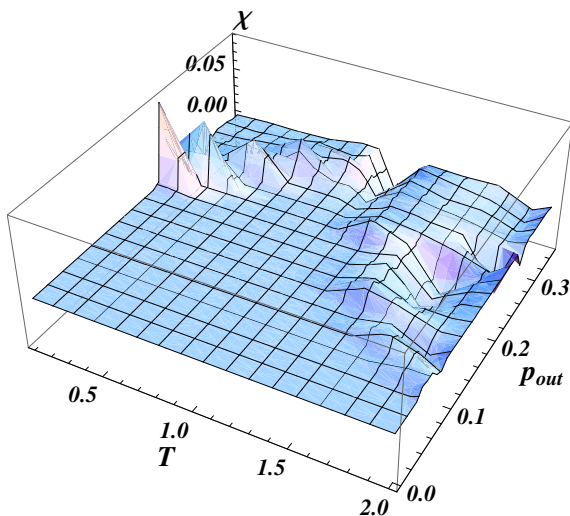


Fig. 11. A measure of the computational complexity χ of the community detection problem as a function of the temperature T and the density of inter-community links p_{out} .

olved two-dimensional defects (dislocations, interstitials, etc.) and domain walls in a lattice. Defects in triangular lattices occurred most frequently near cluster boundaries.

We also tested static configurations for the ternary model glass system where each replica is a model of the same configuration. There we detected structures in both low and high temperatures where the high temperature “structures” are more fragile (that is, harder to solve in the clustering problem). This corresponds to identifying relevant transient features in a dense liquid.

5.1 Ternary model glass results

In Figs. 6 and 7, panels (a) and (b) show the information theory based correlations (averaged over all replica pairs as in [62]) over a range of network resolutions. The lower temperature system at $T = 300$ K in Fig. 6(a) shows a peak NMI at (ia) with a corresponding VI minimum at (ib). Fig. 8 depicts an example of the full system *partition*. Fig. 9 shows some sample clusters within the simulation bounding box at resolution parameter value of $\gamma_{\text{best}} \simeq 0.001$ where we include overlapping node memberships (the replicas correlations are calculated on partitions), and Fig. 10 depicts additional samples of the best clusters. The corresponding high temperature ($T = 1500$ K) solutions have a much lower NMI at $\gamma_{\text{best}} \simeq 0.001$ indicating significantly worse agreement among replicas. That is, one would expect that the high temperature system $T = 1500$ K is in a liquid state, so any observed features are not dynamically stable across all replicas (snapshots of the system over time). At $T = 300$ K, the best structures have consistent cluster sizes that are exclusively MRO.

The plateau regions for $\gamma > 10$ are similar to the LJ plot in Fig. 12, but in this system the NMI plateau is lower. In the high temperature case in Fig. 7, there are additional “almost-plateaus” for the range $0.001 \lesssim \gamma \lesssim 0.1$. These plateaus represent a region of structural transition, but we are not concerned with them because the replica correlations are very low.

5.2 Binary Lennard-Jones glass results

In Figs. 12 and 14, panels (a) and (b) show the data for the replica information correlations over a range of network resolutions. The lower temperature system at a temperature of $T = 5$ (in units of $k_B = 1$) in Fig. 6(a) shows a plateau in NMI at (ia) with a corresponding VI plateau at (ib) which are the local extrema ($V = 0$ is a trivial solution with only one cluster in this problem). Fig. 13 depicts a sample of the best clusters, including overlapping node memberships, at resolution (i) for $\gamma_{\text{best}} \simeq 10^4$. The corresponding higher temperature solutions at $\gamma_{\text{best}} \simeq 10^4$ (see Figs. 14 and 15) have a lower NMI (indicating a weak agreement among replicas). The dependence number of replicas (See Fig. 15) required to achieve high accuracy underscores the faint agreement between contending solutions and the high temperature complexity of the problem. Our identified structures for this LJ model system

are consistent in terms of the cluster sizes and are almost exclusively SRO configurations with simple adjunct-type atoms extending into the low end of MRO size structures.

6 Conclusions

Our method is a new and very general approach to determine the natural multi-scale structures of complex physical systems. We do not bias the expected configurations in any way. The required input is that of inter-particle interactions (or measured correlations as further detailed in Appendix N). Information theory extrema (including plateaus) between contending solutions give the different pertinent structures on all important length scales (lattice scales and correlation lengths) of the system in an unbiased unified way.

Apart from benchmarks on general networks and on lattices and spin systems with and without defects (see Appendices O,P,Q), to illustrate the feasibility of this approach, we focused in this work on structural glasses. The detection of structure in structural glasses is a heavily investigated hard problem. By the use of our method, we identified consistent SRO or MRO structures at temperatures below the glass transition in two different model

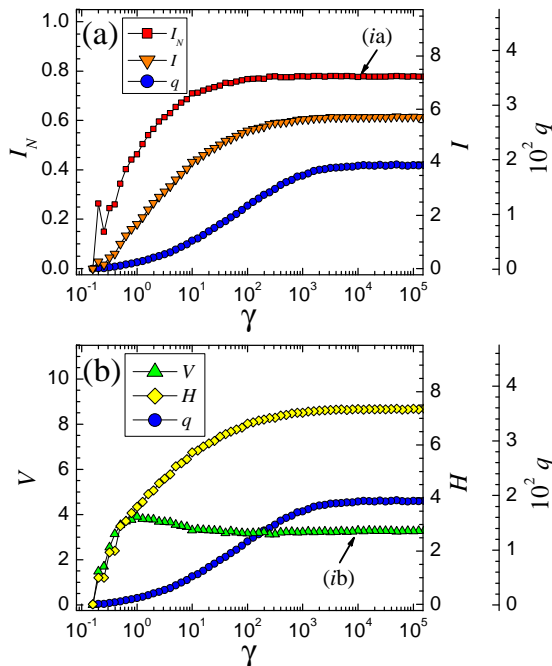


Fig. 12. Panels (a) and (b) show the plots of information measures I_N , V , H , and I and the number of clusters q (right-offset axes) versus the Potts model weight γ in Eq. (3). The LJ system contains 2000 atoms in a mixture of 80% type A and 20% type B (Kob-Andersen binary LJ system [86]) with a simulation temperature of $T = 0.01$ (energy units) which is well below the glass transition of $T_c \simeq 0.5$ for this system. This system shows a somewhat strongly correlated set of replica partitions as evidenced by the information extrema at (ia,b) in panels (a) and (b). A set of sample clusters for the best resolution at $\gamma = 10^4$ is depicted in Fig. 13.

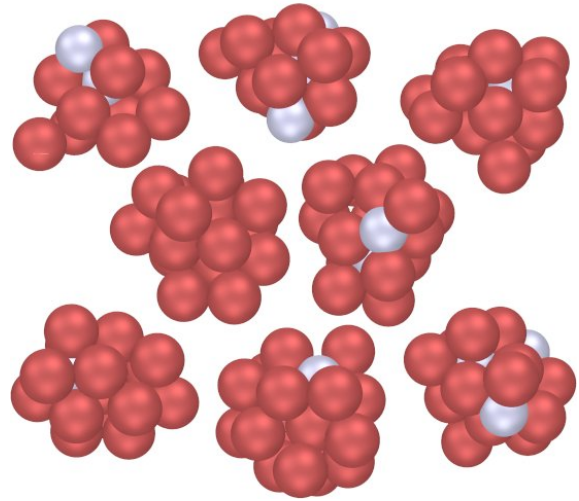


Fig. 13. Several of the best clusters for the peak replica correlation at feature (i) in Fig. 12. These clusters include overlapping node membership assignments where each node is required to have an overall negative binding energy to the other nodes in the cluster. The atomic identities are B (silver) and A (red) in order of increasing diameters.

glass formers. Our analysis evaluates structures in terms of the potential energies (i.e., the internal binding energies of the clusters). This approach differs from some other methods of structural analysis that look strictly at the relative atomic positions. We briefly comment on the relation between our work and that of simpler mode analysis of the interactions – the latter have been indeed been used to detect a link between spatial structure and local dynamics [53,95]. Local heterogeneous dynamics was shown to be correlated with topological defects [96] and thus (as a consequence of [53,95]) with the system modes. (Indeed, a recent work [97] directly reaffirms such a connection.) Similarly, some old variants of graph partitioning methods such as direct spectral clustering [98,99] as well as community detection employ a normal mode analysis [71]. Indeed, a method based on particle dynamics in high dimensions enabled multi-scale community detection [72]. Other different yet conceptually related approaches also include oscillator synchronization analogies [100,73]. In the above approaches, physical analogies were made. It is thus natural to suspect that the approach may be inverted and that community detection will link spatial structure with dynamics in a broad class of physical systems where the physics based analysis of the interacting multi-particle system is hampered by the sheer complexity of the problem. The current work indeed fleshes out this link in detail and introduces a method for the direct detection of general spatio-temporal structures in rather general physical systems. Notably, via the use of information theory correlations and extrema as a function of the Hamiltonian parameters therein (γ of our defining Hamiltonian of Eq. 3 and ϕ_0 of Sect. 5), we are able to identify in an unbiased way *all of the natural scales* of the system. In more rudimentary approaches this needs to be introduced by hand (e.g., a cutoff on mode occupancy in spectral based

approaches) and it is not obvious how to determine all pertinent structures of a complex physical system.

Our approach identifies MRO as the dominant feature of our ternary model glass former with no strongly defined SRO. In contrast, the LJ system shows a largely SRO structure with adjunct atoms that create near-MRO structures. Compounding the changes in structure that we find by analyzing the atomic system at different temperatures and minimizing the energy function to determine the optimal division into clusters, there are also *entropic effects*. The distribution of optimal partitions becomes wider and less pronounced due to these effects as the temperature increases. This is a validation of our arguments in Sect. 4.3.1.

On a lattice, plateaus in information theory correlation steps correspond to a cascade of structures starting from the smallest dyads of nodes, to basic plaquette structures (square, triangle, etc.), and growing ever larger (two joined plaquettes etc.). In Ising spin systems at different temperatures on a square lattice, the domains of “+” and “-” spins are separated from one another by domain walls. The information theory plateaus correspond similarly to the cascade of small plaquette structures found on the lattice itself (*i.e.*, the single plaquette, two joined plaquettes etc.) up to a cutoff scale set by the domain wall. This is sensible since no clear structure is found beyond the domain

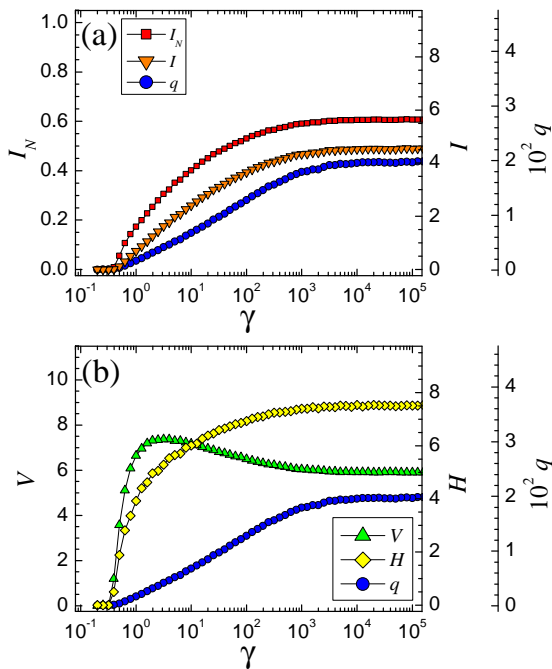


Fig. 14. Panels (a) and (b) show the plots of information measures I_N , V , H , and I and the number of clusters q (right-offset axes) versus the Potts model weight γ in Eq. (3). The LJ system contains 2000 atoms in a mixture of 80% type A and 20% type B (Kob-Andersen binary LJ system [86]) with a simulation temperature of $T = 5$ (energy units) which is well above the glass transition of $T_c \simeq 0.5$ for this system. At this temperature, the replicas are significantly less correlated than the corresponding low temperature case in Fig. 12.

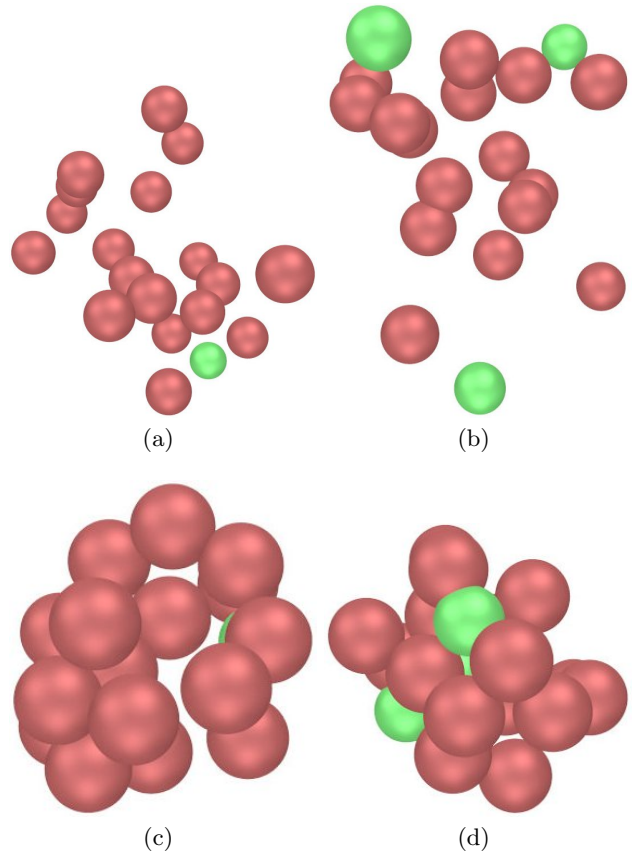


Fig. 15. A sample depiction of dispersed clusters for the LJ system Eq. (2) at a temperature of $T = 5$ (in units where $k_B = 1$). The shown clusters correspond to the multiresolution plot in Fig. 14 at value of the resolution parameter of $\gamma = 10^4$. These clusters are a sample of high temperature counterparts to the low temperature clusters in Figs. 12 and 13. Panels (a) and (b) show a more typical example of dispersed clusters at a number of replicas $s = 10$. In some cases, the identified high temperature clusters can be more compact, but not densely packed. Panels (c) and (d) provide sample solutions for $s = 20$ replicas. An increasing replica (s) number (and generally also trial (t) number, see text) required to achieve better solutions is indicative of a greater computational complexity of the system. Physically, a larger time is required for the system to realize better clusters under ideal conditions (in the absence of quenching and any relaxation time constraints). *The sparsity of the identified clusters in this high temperature system is generally consistent across all clusters in the network solution.* (This lies in contrast to the more compact and more strongly correlated structures found at low temperatures.) The atomic identities are B (silver) and A (red) in order of increasing diameters.

length scale. The largest fluctuations occur at the boundaries between different domains. These domain walls are directly attained by the extrema (those corresponding to the *maximum* in VI). Physically, they correspond to the scales at which the largest fluctuations occur where the large fluctuations lead to poor information theory correla-

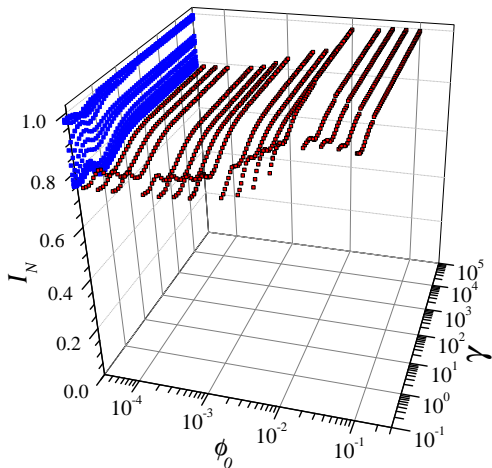


Fig. 16. Plot of NMI I_N as a function of the potential shift ϕ_0 and the Potts model weight γ for the ternary model system in Sect. 5.1. The temperature is $T = 300$ K which is *below* the glass transition temperature for this system. This plot shows that the peak is roughly constant across a range of potential shifts. In general systems, we can obtain all natural scales by shifting both ϕ_0 and γ and looking for extrema (and plateaus in some cases, see Sect. O). See Fig. 6 for the corresponding 2D plot using $\phi_0 = \phi_{avg}$.

tions between the different replicas. Fig. 42 corresponds to a sample depiction of the system at the *maximum* VI. The correlation lengths – set by the scale of the largest domain walls – are thus related to the scale which the fluctuations in the information theory overlaps are maximal (as manifest via *maxima* in VI).

As we detail in Appendix S, a general rigid amorphous solid supports shear and a divergent “shear penetration length”. This length scale monotonically increases as a liquid is cooled to form a rigid glass. Within our graph theoretic method, we may employ the shear stress correlations as to represent graph weights to analyze such behavior.

ACKNOWLEDGMENTS

We are indebted to M. Widom and M. Mihalkovič for help with effective atomic potentials and to ongoing work [102], to Wolfgang Weiser for the 2D Ising lattice simulation code made available on his website. This work was supported in part by the LDRD DR on the physics of algorithms at LANL and the Center for Materials Innovation at Washington University in St. Louis. ZN thanks N. Goldenfeld, Z. Rotman, G. Tarjus, and P. G. Wolynes for helpful comments. He also wishes to thank the KITP and the Lorentz Center for hosting stimulating workshops.

A Information theory measures

We utilize the variation of information [76] and normalized mutual information to measure the strength of the

correlations among the independent replicas in our multiresolution algorithm. The mutual information $I(A, B)$ between community divisions A and B is

$$I(A, B) = \sum_{i=1}^{q_A} \sum_{j=1}^{q_B} \frac{n_{ij}}{N} \log \left(\frac{n_{ij}N}{n_i n_j} \right). \quad (5)$$

q_A and q_B are the number of communities in divisions A and B , n_i and n_j are the number of nodes in communities i and j , and n_{ij} is a “confusion matrix” that identifies the number of nodes in community i of partition A that are found in community j of partition B . For a single community division A , we can determine the self mutual information by $H(A) = I(A, A)$ which is identically equal to the Shannon entropy. We use base 2 logarithms.

We calculate the variation of information $V(A, B)$ by

$$V(A, B) = H(A) + H(B) - 2I(A, B). \quad (6)$$

The range for VI is $0 \leq V(A, B) \leq \log N$. The normalized mutual information $I_N(A, B)$ is

$$I_N(A, B) = \frac{2I(A, B)}{H(A) + H(B)}. \quad (7)$$

The range for NMI is $0 \leq I_N(A, B) \leq 1$. The NMI and VI afford slightly different perspectives on the replica correlations in the multiresolution analysis above.

These information measures are based on the cluster definitions and are not directly related to a thermodynamic entropy. The replica correlation measures could be improved by incorporating information about the assigned “overlapping” configurations (nodes may belong to more

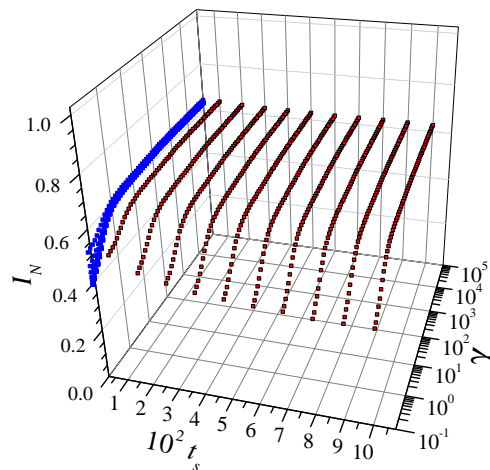


Fig. 17. Plot of NMI I_N as a function of the time (MD time steps) between configurations t_s and the Potts model weight γ for the ternary model system in Sect. 5.1. The temperature is $T = 1500$ K which is *above* the glass transition temperature for this system. Intuitively, this plot shows that the correlations become weaker as the time between configurations is increased. This process of examining the correlations as a function of t_s and γ allows us to examine the relevant time scales in addition to the natural spatial scales that we identify in Sect. 5.

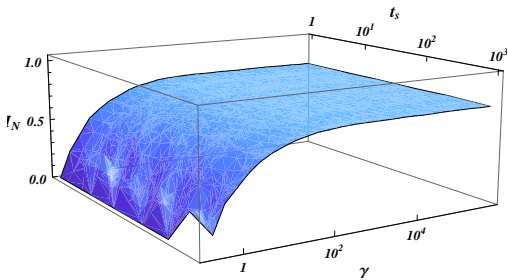


Fig. 18. Plot of NMI I_N as a function of the time (units of 10 MD time steps) between configurations t_s and the Potts model weight γ for the ternary model system in Sect. 5.1. The temperature is $T = 0.01$ which is *above* the glass transition temperature for this system. Intuitively, this plot shows that the correlations become weaker as the time between configurations is increased. Intuitively, this plot shows that the correlations become weaker as the time between configurations is increased.

than one cluster) such as in Ref. [92], by modifying the measures to account for the fact that same-type atoms are indistinguishable in this type of a model, or by utilizing a thermodynamic entropy since we are dealing with a physical system in the current application.

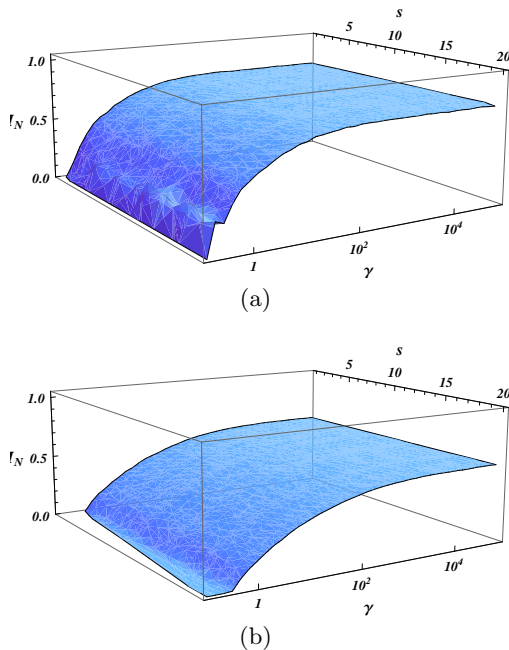


Fig. 19. Plot of NMI I_N as a function of the number of trials s used to optimize the solution and the Potts model weight γ for the binary LJ system in Sect. 5.1. The temperatures are $T = 0.01$ in panel (a) and $T = 5$ in panel (b). The number of trials has a higher effect on the accuracy in the $T = 5$ system, but the number of trials does not result in a drastic improvement to the accuracy of our algorithm for either LJ system.

B Physical community detection models

Minimizing the Hamiltonian of Eq. (3) using the algorithm briefly explained in Sect. 4.2, models a dynamic community detection process where we search for a local energy minimum that indicates a “good” community partition (in general). In particular, we have applied a potential energy (PE) model of network edges, and we could, in principle, apply other edge definitions to obtain other relevant configurations with the following caveat. When we minimize the Hamiltonian using the edge weights, a low energy state corresponds to a good partition, so for consistency with the community detection problem, any edge definitions should ideally be extremized at the most favorable configuration(s). The subtle distinctions between a few different natural edge weight models can result in different calculated clusters (beyond natural fluctuation caused by a high configurational entropy).

An inverted PE model fits the above criterion, and it would at first appear to be conceptually consistent with a model based on the relative pairwise squared node displacement (SND) model. For both cases, small deflections about the minimum still indicate a good, even if not optimal, configuration corresponding to the intuitive notion of a bound cluster. However, the SND model would cause a perfect crystal to be identified as a single contiguous cluster. The PE would not have this effect since more distant nodes have a much lower potential energy. In effect, the PE model could identify the smaller scale units in a perfect crystal that the SND model could not isolate.

Another intuitive edge model for bound clusters is related to the attractive force that one may expect to exist between constituent elements of a physical cluster. Of course, the system forces still cause the formation of a crystalline ground under the appropriate conditions, but the forces dictate the system’s physical *dynamics* over time where the PE model (more) directly indicates the relevant ground state(s). Forces with a minimum such as the LJ model in Eq. (2) would be zero at the optimal ground state configuration (ideal crystal state), and the maximum force would be at a larger radius r than the PE minimum. While a force model of edge weights is also intuitive, it would correspond to (perhaps slightly) different clusters in a physical system compared to clusters derived from a PE model because the community detection Hamiltonian is extremized at different radii.

This discussion of the subtle differences between the edge models leads to the natural question of which is the “best” physical cluster model. Another perspective is that the different edge weight models simply answer different questions. We have selected the PE definition since it best corresponds to the ideal ground state of the system in our pairwise interaction model. We then infer the best local clusters within configurations in local (frustrated) equilibrium (in the solid systems).

C MRO and structure factor pre-peaks

One experimental approach to ascertain MRO is to look for “prepeaks” in the scattering data. That is, one can look for lower amplitude peaks in the structure factor $S(q)$ which precede the dominant $S(q)$ peak for wavenumbers q . While the approach may capture general MRO structures, it is possible to have MRO structures *without significant pre-peak(s)* in the structure factor plot.

We illustrate the basic premise of this statement with an elementary example – that of a random arrangement of crystallites. Even though the Fourier transform of the mass density in each individual crystallite has sharp peaks at the reciprocal lattice vectors corresponding to these small crystallites, the structure factor obtained from the entire system may have those peaks vanish. We may, for instance, denote the locations of the centers of mass of individual grains i by \mathbf{R}_i and denote the location of individual atoms j in each grain with respect to its center of mass by \mathbf{r}_j . In that case, the structure factor is

$$S(\mathbf{k}) = \sum_{\mathbf{R}_i} \sum_{\mathbf{r}_j \in i} \exp[i\mathbf{k} \cdot (\mathbf{R}_i + \mathbf{r}_j)]. \quad (8)$$

Within each individual grain on its own,

$$S_i(\mathbf{k}) = \sum_{\mathbf{r}_j \in i} \exp[i\mathbf{k} \cdot (\mathbf{R}_i + \mathbf{r}_j)] \quad (9)$$

will be sharply peaked about the corresponding reciprocal lattice vectors of grain i . However, the complete sum,

$$S(\mathbf{k}) = \sum_{\mathbf{R}_i} \exp(i\mathbf{k} \cdot \mathbf{R}_i) S_i(\mathbf{k}), \quad (10)$$

may vanish if the relative distances between the different crystallites are random and lead to phases $\exp(i\mathbf{k} \cdot \mathbf{R}_i)$ which obliterate the signatures of order in the individual $S_i(\mathbf{k})$.

D Overlapping nodes between different communities

We wish to account for the possibility of a given atom being connected to more than one physical cluster. For example, in a cubic lattice, each atom participates in the local structure of multiple unit cells. In community detection, this corresponds to allowing “overlapping” community memberships where a node can be a member of more than one community. To accomplish this task, we select the lowest energy partition at the best resolution(s) of the model network [*i.e.*, value(s) of γ in Eq. (3) corresponding to extrema in I_N or V].

First, we fix the initial node memberships including the number of communities q . We then sequentially iterate through the community memberships of each node and make changes according to the following: (1) place the node in any additional (non-member) clusters to which it

is bound (a negative energy contribution), or (2) remove the node from any member clusters (except for the original membership) in which the current net energy contribution is positive. This process iterates through all nodes as many times as necessary until no node additions or removals are found. The total computational cost is slightly higher than the initial partitioning cost in Sect. 4.2 due to the multiple allowed memberships. See also [92] for another method that allows overlapping multiscale network analysis in a general fashion.

E Potential shift in the ternary metallic glass

In Fig. 16, we show the NMI correlations for a range of potential shifts ϕ_0 and the Potts model weights γ using $s = 12$ replicas and $t = 10$ trials for all data. The NMI peaks are roughly constant over a range of ϕ_0 for the ternary model glass up to $\phi_0 = 0.1$ (the A-A interaction minimum $\phi_{\min} \simeq 0.24$ eV).

F Time correlations in the ternary model glass

In Fig. 17, we show the NMI correlations for a range of separation times t_s between replicas (units are in MD time steps) and the Potts model weights γ using $s = 12$ replicas and $t = 10$ trials for all data. This plot intuitively shows that the correlations weaken as we increase the separation

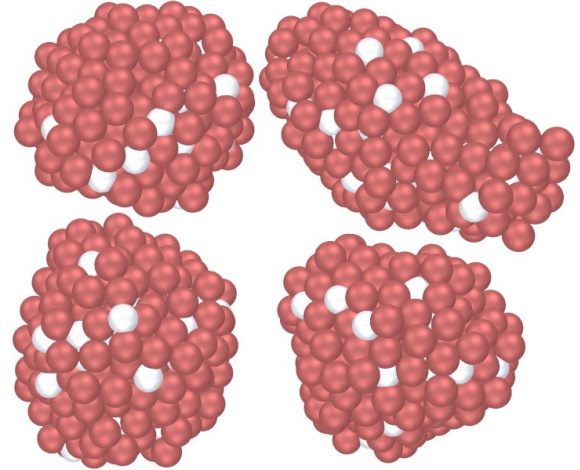


Fig. 20. Some of the best clusters for the peak V for the low temperature system shown in Fig. 12 in panel (b). The peak in the variation of information V generally correlates with the scale on which the fluctuations in the system division are most prominent. These clusters include overlapping node membership assignments where each node is required to have an overall negative binding energy to the other nodes in the cluster. The atomic identities are B (silver) and A (red) in order of increasing diameters. The resulting configurations constitute tightly bound objects. Representative corresponding high temperature clusters are shown in Fig. 21.

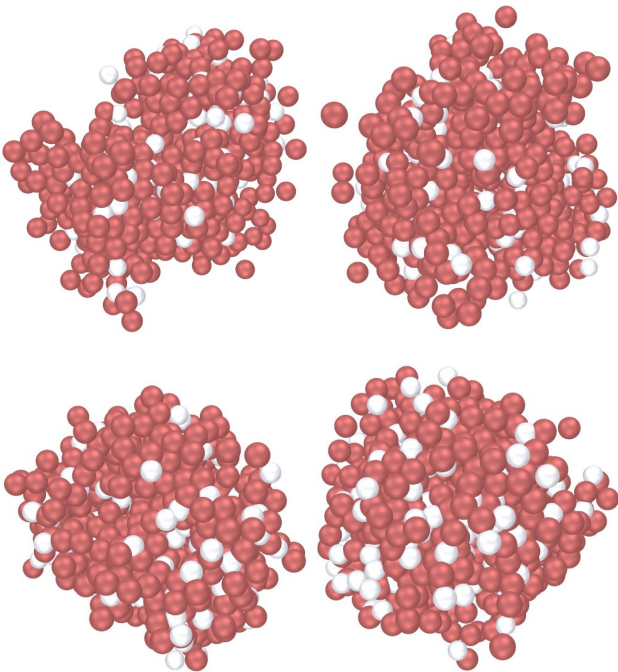


Fig. 21. The best clusters found for the peak V for the replica correlation within the high temperature LJ system (see text). These clusters include overlapping node membership assignments where each node is required to have a overall negative binding energy to the other nodes in the cluster. The peak in the variation of information V generally correlates with the scale on which fluctuations are the largest. The atomic identities are B (silver) and A (red) in order of increasing diameters. The diffuse objects found at high temperatures are no longer as compact as at lower temperatures. The normalized mutual information at the peak V is also correspondingly lower than that for the low temperature system.

time between replicas. Through varying the time step between replicas, we examine the correlations as a function of t_s and γ which allows us to determine the most important time scale(s) (or relative equivalence). See Fig. 6 for the corresponding 2D plot using $t_s = 1000$, and the static limiting case is shown explicitly in Sect. K.

G Time correlations in the binary LJ glass

In Fig. 18, we show the NMI correlations for a range of separation times t_s between replicas (units are in MD time steps) and the Potts model weights γ using $s = 12$ replicas and $t = 10$ trials for all data. This plot shows that the correlations weaken only a little as we increase the separation time between replicas up to 10 000 MD time steps. Through varying the time step between replicas, we examine the correlations as a function of t_s and γ which allows us to determine the most important time scale(s) (or relative equivalence). See Fig. 6 for the corresponding 2D plot using $t = 1000$, and the static limiting case is shown explicitly in Sect. K.

H An optimization effect in the binary LJ glass

In Fig. 19, we show the NMI correlations for a range of optimization trials t for $s = 12$ replicas and the Potts model weights γ . The plots show that the number of trials t has a small effect on the overall accuracy of the solution for either temperature ($T = 0.01$ or 5), but the effect is slightly more pronounced in the higher temperature $T = 5$ case. See Figs. 12 and 13 for the corresponding 2D plots using $s = 10$.

The high temperature clusters are generally much more dispersed. See Fig. 15 for sample clusters using $t = 10$ and 20 at $T = 5$ where the clusters correspond to the multiresolution plot in Fig. 14 at $\gamma = 10^4$. The corresponding low temperature clusters are analyzed Fig. 12 and presented in Fig. 13. Panels (a) and (b) in Fig. 15 display the typical case of dispersed clusters at $t = 10$. In some instances, the high temperature clusters can be more compact, albeit not densely packed, where panels (c) and (d) show two examples at $s = 20$. The clusters that are identified are generally consistent in terms of sparseness across all clusters in the solution. The frequency of occurrence of the more compact high temperature clusters, and its dependence on the level of optimization, is a subject for further study.

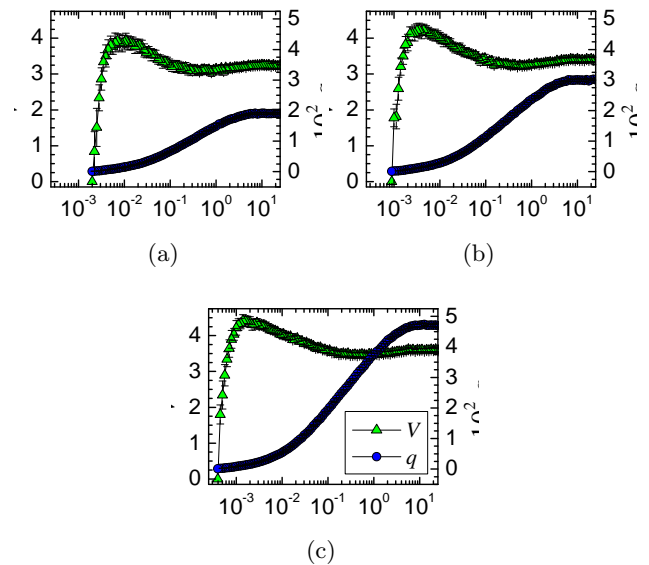


Fig. 22. Plots of the variation of information V between replica pairs as a function of the resolution parameter γ for several system sizes in a LJ simulation (see Sect. 3.2). Panels (a), (b), and (c) use $N = 2000$, $N = 4000$, and $N = 8000$, respectively. Note that the value of γ corresponding to the peak V scales downward with the system size (larger structures) which may indicate that it is correlated to a diverging length scale.

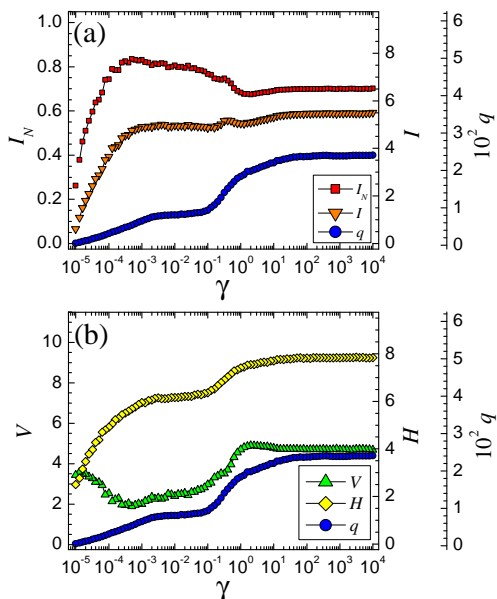


Fig. 23. Panels (a) and (b) show the plots of information measures I_N , V , H , and I and the number of clusters q (right-offset axes) versus the Potts model weight γ in Eq. (3). The ternary model system contains 1600 atoms in a mixture of 88% type A, 7% of type B, and 5% of type C with a simulation temperature of $T = 300$ K which is well *below* the glass transition for this system. In this system, we use a single *static* “snapshot” of the system to analyze what our multiresolution algorithm finds at $T = 300$ K. This low temperature case shows a preferred resolution at low γ as evidenced by the information extrema at (i) in both panels. See Fig. 24 for the corresponding high temperature case.

	a_0	a_1	a_2	a_3	a_4	a_5
AA	2.11*	9.49*	-32.3*	3.66*	-10.6*	6.20*
AB	1.92	17.4	6.09	3.05	-4.68	3.48
AC	2.38	8.96	-14.9	3.11	-3.88	4.38
BB	2.01*	4.95*	5.01*	2.74*	-2.26*	3.00*
BC	1.88	8.00	-3.42	2.53	-1.25	3.00
CC	2.75*	15.3*	-6400*	2.38*	-4.69*	8.71*

Table 2. Fit parameters for Eq. (1) obtained from fitting configuration forces and energies to ab-initio data [83,84]. The units of the parameters are such that given r in Å, $\phi(r)$ is in eV. The same-species (*) data is different from Table 1.

I Multiresolution VI maxima in the LJ system

In Fig. 12, we show the multiresolution correlations as a function of the Potts model weight γ for a LJ system of $N = 2000$ nodes using $s = 12$ replicas and $t = 10$ trials for all data. The value of γ corresponding to the peak in V corresponds to the “maximum complexity” of the energy landscape which is often correlated to the system size (see Appendix J). Fig. 20 shows a sample of the best clusters corresponding to the VI peak which are roughly 300 atoms in size (7 – 8 atoms in diameter) which is approximately 1/7 of the size of the system. Fig. 21 shows some corresponding high temperature $T = 5$ clusters which we

note are approximately twice the size ($n \simeq 600$ nodes) and more dispersed.

As an additional note, we remark that, intuitively, one would expect that the VI maxima are directly related to the NMI minimum in this region of γ . This is not the case in this region because the VI metric does to zero as the network collapses to one cluster. It is rapidly shifting from a region of maximum complexity at a peak VI value, where most of the information comes from the sum of the Shannon entropies $H(A)$ and $H(B)$, for two partitions A and B , to minimum complexity at a value of $V = 0$. NMI has a different behavior here, as the ratio $I_N = 2I(A, B) / [H(A) + H(B)]$, because the mutual information between different replicas becomes smaller and approaches zero as the system collapses into larger communities. The low temperature LJ system in Fig. 12 shows a transitional very low peak in NMI which corresponds to a near bisection of the system. However, in this case the overlapping cluster configurations collapse to the entire system.

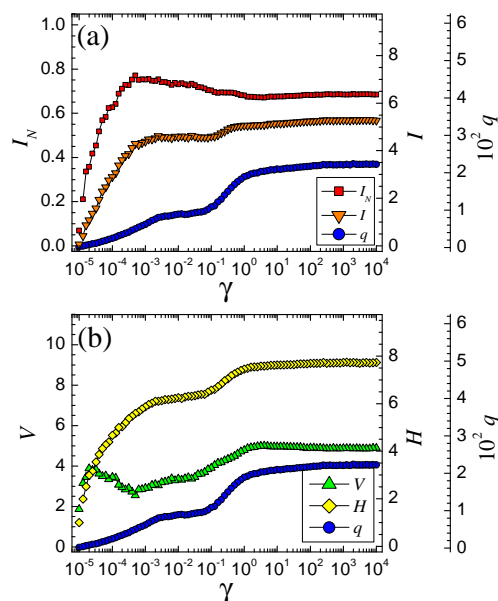


Fig. 24. Panels (a) and (b) show the plots of information measures I_N , V , H , and I and the number of clusters q (right-offset axes) versus the Potts model weight γ in Eq. (3). The ternary model system contains 1600 atoms in a mixture of 88% type A, 7% of type B, and 5% of type C with a simulation temperature of $T = 1500$ K which is well *above* the glass transition for this system. In this system, we use a single *static* “snapshot” of the system to analyze what our multiresolution algorithm finds at $T = 1500$ K. This high temperature case does show a preferred resolution at low γ as evidenced by the information extrema at (i) in both panels, but the NMI maxima are somewhat lower. The solutions also take longer to solve accurately meaning that the community detection energy landscape is more complicated. See Fig. 23 for the corresponding low temperature case.

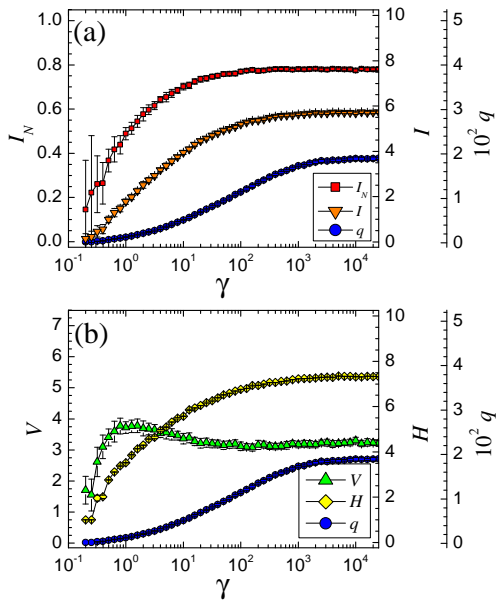


Fig. 25. Panels (a) and (b) show the plots of information measures I_N , V , H , and I and the number of clusters q (right-offset axes) versus the Potts model weight γ in Eq. (3). As in Sect. 5.2, this LJ system contains 2000 atoms in a mixture of 80% type A and 20% type B with a simulation temperature of $T = 0.01$ (energy units) which is well *below* the glass transition for this system. In this test, we use a single *static* “snapshot” of the system. This low temperature system has a higher overall level of correlation among the replicas than the high temperature case in Fig. 25, and the overall results are very similar to what was observed for the time separated replicas in Fig. 12 in Sect. 5.2. See Fig. 27 for a sample of some of the best observed clusters.

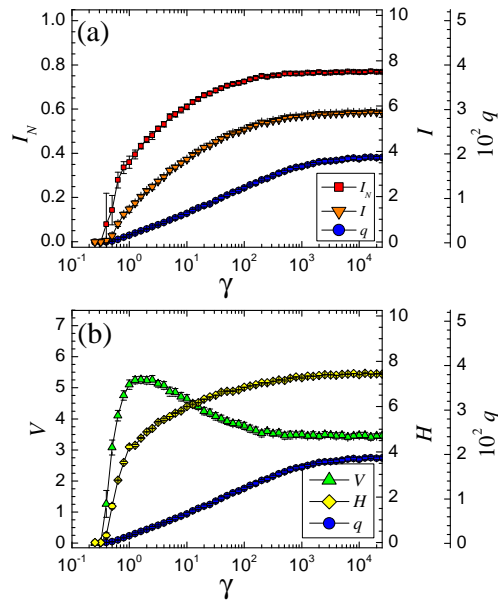


Fig. 26. Panels (a) and (b) show the plots of information measures I_N , V , H , and I and the number of clusters q (right-offset axes) versus the Potts model weight γ in Eq. (3). The LJ system contains 2000 atoms in a mixture of 80% type A and 20% type B with a simulation temperature of $T = 5$ (energy units) which is well *above* the glass transition for this system. In this analysis, we use a single *static* “snapshot” of the system. This high temperature system has a lower overall correlation than the low temperature case in Fig. 25, and the overall results are very similar to what was observed for the time separated replicas in Fig. 14 of Sect. 5.2.

J Finite size effects in the LJ system

In Fig. 22, we show the VI correlations as a function of the Potts model weight γ for several system sizes of $N = 2000$, $N = 4000$, and $N = 8000$ in panels (a), (b), and (c), respectively. We also used $s = 12$ replicas and $t = 10$ trials for all data. The value of γ corresponding to the peak in V scales downward with the system size (larger structures) indicating that the maximum fluctuations are scaling with the size of the simulation box. In the limit of an infinite size simulation box, the VI peak would tend to $\gamma = 0$.

K Static Multi-resolution analysis on ternary model glass

The inter-replica NMI/VI correlations change with the time separation interval between the replicas where the longer time separations intuitively result in poorer correlations. The other limiting case is for a *static* analysis of the system. Thus, we are interested in determining what our multiresolution analysis finds when we examine a single-time snapshot of the system. A single snapshot may, potentially, capture a transient feature of the system. This

is illustrated in panel (a) of Fig. 4 in which the time separation between different replicas is set to zero. We applied the same algorithm as in Sect. 4 except that all replicas correspond to the same system time, and we solved the systems with $s = 8$ replicas and $t = 4$ trials per replica. In Figs. 23 and 24, our analysis identifies a *static length* associated with the instantaneous configuration. At both high and low temperatures, the static multi-resolution analysis display information extrema at low γ (large spatial scales). The higher temperature system displays weaker correlations with sparser structures whereas the structures of the low temperature system display more significant correlations (and more compact structures). As seen in Figs. 23 and 24 the high temperature system displays weaker correlations in the vicinity of the peak NMI than those of the low temperature system. That is, the high temperature solutions require more effort to solve accurately (there are far more metastable minima and more trials are required in order to find better contending solutions). (A similar occurrence was found for the high temperature LJ system in Fig. 15.) The solved clusters (not depicted) are comparable to those identified for the time-separated replicas in Sect. 5 for both system temperatures.

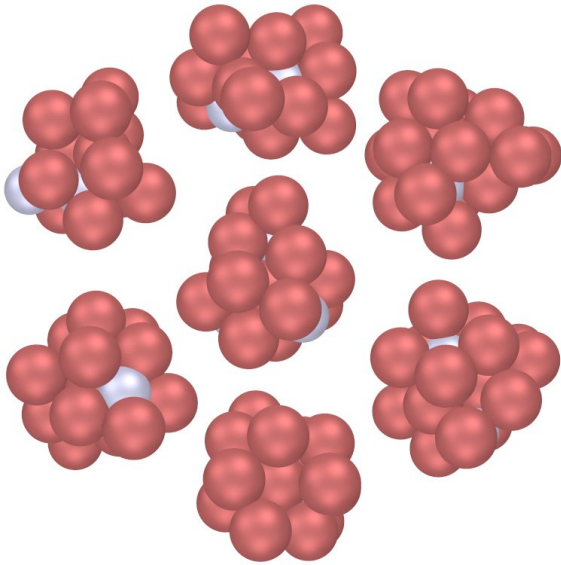


Fig. 27. A depiction of some of the best clusters for the peak replica correlation in the static system of Fig. 25. These clusters include overlapping node membership assignments where each node is required to have an overall negative binding energy to the other nodes in the cluster. The atomic identities are A (red) and B (silver).

L Static Multi-resolution analysis on LJ glass

As in Appendix K for the ternary system, we further tested a static version of the binary LJ model where the results are similar to the dynamic case in Sect. 5.2 both in the MRA plot and the resulting clusters. A notable exception is that the distinction between the high and low temperature cases becomes more subtle in the multi-resolution plots.

We applied the same algorithm as in Sect. 4 except that all replicas correspond to the same system time, and we solved the systems with $s = 12$ replicas and $t = 10$ trials per replica. In Figs. 25 and 26, we show our multi-resolution analysis associated with the instantaneous configurations. These two static plots are similar, but the high temperature case has slightly weaker correlations (lower NMI peak and higher VI minimum). In Figs. 25 and 26 where we use time separated replicas, the contrast in the MRA plots at different temperatures is stronger. Fig. 27 shows a sample of the best clusters in the low temperature case which are comparable to those identified for the time-separated replicas in Fig. 13 in Sect. 5.2.

M An analysis of yet another ternary system

In Figs. 28 and 29, we repeat the analysis of Sects. 3.1 and 5.1, for an alternate ternary model glass system (AlYFe). In particular, we use the best parameter fit for the same-species interactions that are tabulated in Table 2 as opposed to implementing the GPT [85] as used in Figs. 6 – 10 and tabulated in Table 1. A plot of the alternate po-

tentials is shown in Fig. 30. These interactions conform to those

The lower temperature system at $T = 300$ K in Fig. 28(a) shows a peak NMI at (ia) with a corresponding VI minimum at (ib). Following Sect. 5.1, Fig. 31 depicts a sample of the best clusters at $\gamma_{best} \simeq 0.001$ where we include overlapping node memberships (the replica correlations are calculated on partitions). We used $s = 12$ replicas and $t = 20$ trials per replica. The corresponding $T = 1500$ K high temperature solutions have a much lower NMI at $\gamma_{best} \simeq 0.001$ indicating very poor agreement among the replicas. At $T = 300$ K, the best structures have consistent cluster sizes that are MRO or a little larger which are generally larger than $1/2$ the simulated system width. Therefore, it would be beneficial to test the consistency of the clusters in a larger system requiring a substantially longer computational time.

In this system the NMI plateau at $\gamma \gtrsim 100$ is actually higher than the configuration at (i), but the clusters are almost exclusively small ($n \simeq 5$ nodes) and are not completely contiguous. The distinction in the results between the different potential models is likely due to the longer range Al-Al minimum in the ab initio potential parameter fit data as compared to the GPT [85] minimum.

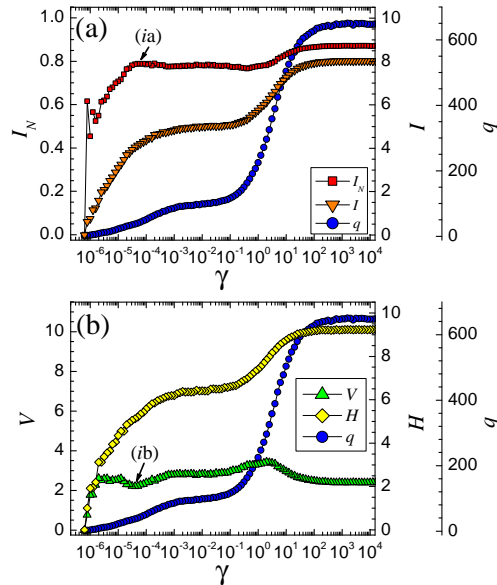


Fig. 28. Panels (a) and (b) show the plots of information measures I_N , V , H , and I and the number of clusters q (right-offset axes) versus the Potts model weight γ in Eq. (3). The ternary model system contains 1600 atoms in a mixture of 88% type A, 7% of type B, and 5% of type C with a simulation temperature of $T = 300$ K which is well below the glass transition for this system. This alternate system uses the best fit parameter data for the same-species interactions as opposed to the pseudo-potential interaction used in Figs. 6 – 10. This system shows a locally preferred resolution as evidenced by the information extrema at (i) in both panels. A set of sample clusters for the best resolution at $\gamma \simeq 0.0001$ is depicted in Fig. 31. The region for $\gamma \gtrsim 100$ actually has a higher correlation, but the clusters are very small ($n \simeq 5$ nodes) and somewhat dispersed.

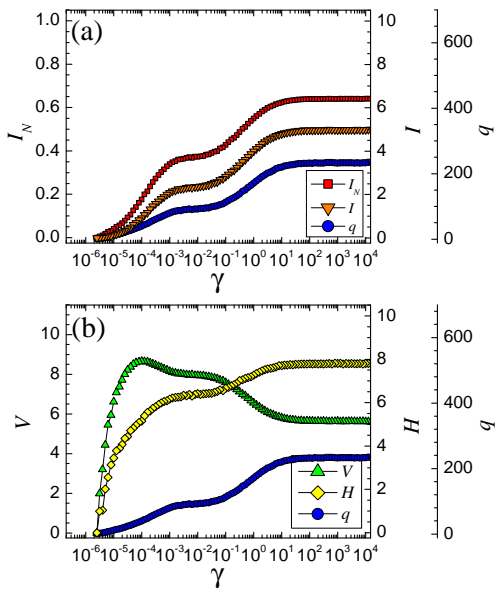


Fig. 29. Panels (a) and (b) show the plots of information measures I_N , V , H , and I and the number of clusters q (right-offset axes) versus the Potts model weight γ in Eq. (3). The ternary model system contains 1600 atoms in a mixture of 88% type A, 7% of type B, and 5% of type C with a simulation temperature of $T = 1500$ K which is well *above* the glass transition for this system. This alternate system uses the best parameter fit for the same-species interactions as opposed to the pseudopotential interaction used in Figs. 6 – 10. At this temperature, there is no resolution where the replicas are strongly correlated. See Fig. 28 for the corresponding low temperature case where the replicas are much more highly correlated at $\gamma \simeq 0.001$.

N Multi-resolution analysis via measured pair correlation function

As stated in Sect. 2, we may apply the same multiresolution network clustering ideas for other structure models. In particular, in Fig. 32, we apply the method to experimentally adduced pair correlation functions $g_{ab}(r)$ in an amorphous ZrPt system between the different of the different components a and b (i.e., Zr-Zr, Zr-Pt, and Pt-Pt). That is, we set in Eq. (3), $A_{ij} = -(g_{ij} + \bar{g}_{ij})$ if $(g_{ij} + \bar{g}_{ij}) < 0$ and $B_{ij} = (g_{ij} - \bar{g}_{ij})$ if $(g_{ij} - \bar{g}_{ij}) > 0$. Here, g_{ij} denotes the pair correlation between the atoms corresponding to nodes i and j , \bar{g}_{ij} is a background average (which we set to zero). Some sample clusters then found by our method are seen in Fig. 33. Due to the large system size, we used $s = 8$ replicas and $t = 4$ trials per replica.

Amorphous systems with extended atomic order beyond the nearest neighbor shell provide an excellent framework to test the identification of natural structural elements. The ZrPt is a system that has been shown to have MRO in both the glassy and liquid state [103, 104, 105, 106, 107]. MRO, or correlations beyond direct chemical bonding manifest as pre-peaks in the static structure factor extracted from scattering studies of liquids and glasses. The dominant structural elements at the heart of such an

ordering are of extreme interest. Atomic configurations that are consistent with the experimentally determined scattering data for liquid $\text{Zr}_{80}\text{Pt}_{20}$ at 250 K below the liquidus were generated using conventional Reverse Monte Carlo (RMC) methods [108, 109, 110]. The result of analysis uses unconstrained RMC which may or may not emulate the precise microscopic structure. We then analyzed a representative system with $N = 7500$ nodes using the algorithm outlined in Sect. 4.3.

Specifically, we analyze the system as a *static* model. That is, each replica is based on the one particular system representation since the data is obtained by RMC methods rather than by a dynamical simulation. The multi-resolution analysis (MRA) is seen in Fig. 32. A few of the relatively uniform large clusters are shown in Fig. 33 where each cluster is approximately 700 – 800 atoms in size. Interestingly, the ZrPt system shows a well-defined secondary MRA NMI peak near $\gamma \simeq 1$. Although the peak NMI value has a poor overall correlation among the replica solutions (low I_N), it is notable that the system displays this secondary peak since it is entirely absent in the LJ binary liquid results in Sect. 5.2.

O Multiresolution application to lattice systems

We define several uniform lattices systems for the purpose of comparing the results to the model glasses where we use relatively small systems for presentation purposes. We would normally just treat respective model networks as unweighted networks, but here we wish to maintain a consistent analysis across all systems in the paper, so we further apply a “potential” shift ϕ_0 which corresponds to

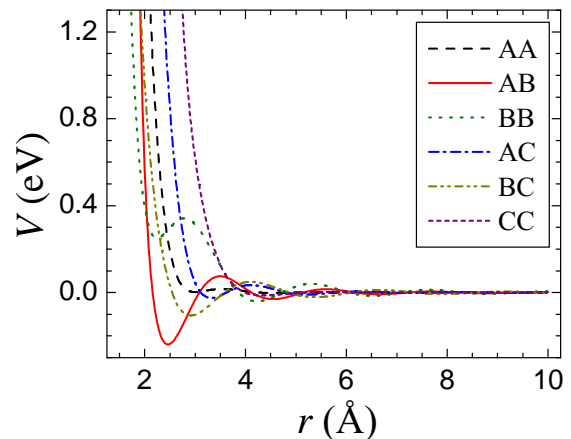


Fig. 30. A plot of the model potentials for our three-component model glass former (see Fig. 1) using the fit data in Table 2. We indicate the atomic types by “A”, “B”, and “C” which are included with mixture ratios of 88%, 7%, and 5%, respectively. The units are given for a specific candidate atomic realization (AlYFe) discussed in the text. Here, we apply the ab initio fit data for the same-species interactions, as opposed to the GPT [85] model from Table 1 in Fig. 2.

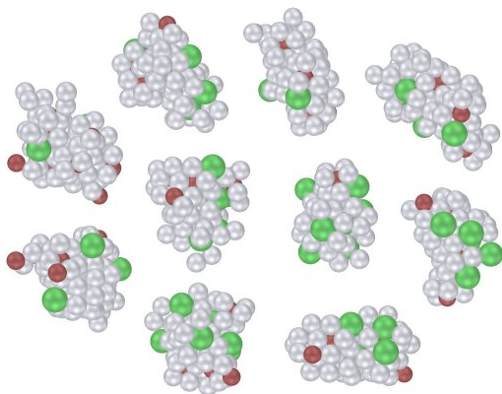


Fig. 31. A depiction of some of the best clusters for the peak replica correlation at feature (i) in Fig. 6. These clusters include overlapping node membership assignments where each node is required to have an overall negative binding energy to the other nodes in the cluster. The atomic identities are C (red), A (silver), B (green) in order of increasing diameters. These clusters are generally larger than $1/2$ the simulated system width; therefore, it would be beneficial to test their consistency in a larger simulation (requiring substantially longer computational time).

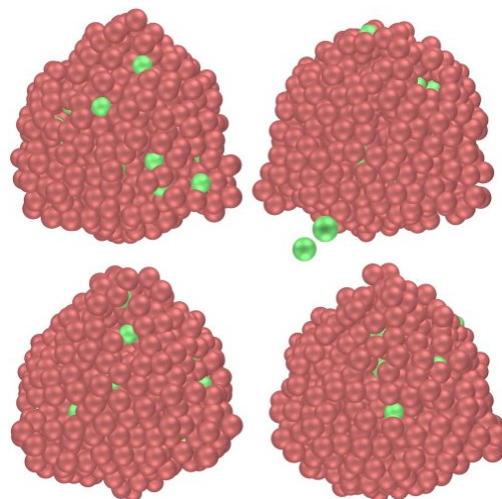


Fig. 33. A sample of clusters determined by a multiresolution clustering analysis based on the pair correlation function in Fig. 32. The system is a $Zr_{80}Pt_{20}$ system at 250 K below the liquidus (see text) where Zr atoms are depicted as red, and Pt atoms are depicted as green. Each cluster has approximately 700 – 800 atoms.

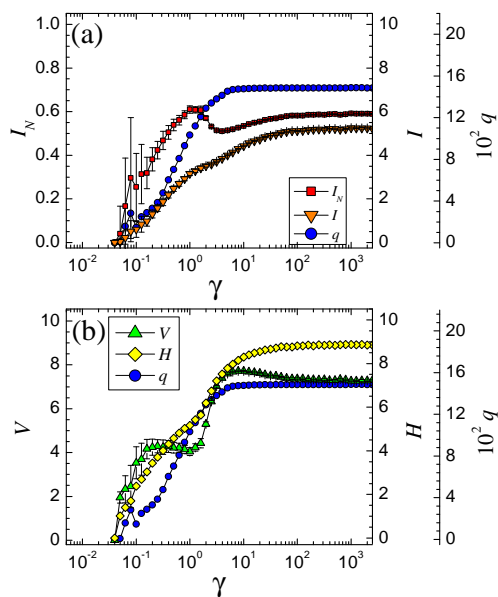


Fig. 32. A plot for the multiresolution analysis of a binary $Zr_{80}Pt_{20}$ system at 250 K below the liquidus. Atomic configurations were generated using conventional RMC methods that are consistent with the experimentally determined scattering data for liquid $Zr_{80}Pt_{20}$ at 250 K below the liquidus. The plot shows a poorly correlated, but nevertheless well-defined, peak in NMI near $\gamma \simeq 1$.

the negative of the average weight over all pairs of nodes (any non-neighbor has a weight of $B_{ij} = 1$).

We allow zero energy moves for the lattice solutions and perform a more strenuous optimization using $s = 20$ replicas and $t = 40$ trials. These representative networks result in “imperfect” tilings of the favored local structures due to the constraints imposed by the perfect symmetry

in the Hamiltonian and by the local solution dynamics. In the depictions, different colors represent distinct clusters (best viewed in color) and edges *between* clusters are made partially transparent as a visualization aid. No overlapping nodes are assigned in the lattice depictions.

0.1 Square lattice

We define a uniform, initially unweighted, square lattice with $N = 400$ nodes. Edges are assigned to each neighbor in the x and y directions with periodic boundary conditions. The “potential” shift is $\phi_0 = 0.97995$. We then perform the same multiresolution analysis to the graph as in the previous systems. In Fig. 34, we see that there are three dominant plateaus in the information measures.

Except for the plateaus, the overall multiresolution pattern resembles the LJ system in Fig. 5.2, except for the presence of the plateaus in the lattice plot, which suggests that the LJ system is “more ordered” than the metallic glass model. However, a purely random graph [62] also shows a similar pattern, including a plateau, which indicates that there may exist an analogy between purely “random” and perfectly “ordered” systems in our analysis. However, these data are not alone sufficient to be conclusive.

We select a configuration at $\gamma = 60$ corresponding to the center plateau. The lattice is depicted in Fig. 35 with $q = 120$ clusters of 78 squares, 4 triads, and 38 dyads. At this resolution, the square dominates the configuration which shows that our algorithm is able to isolate the basic unit cells of the lattice in a natural fashion.

The plateau for $\gamma \gtrsim 100$ corresponds to essentially all dyads, and the plateau for $\gamma \lesssim 30$ corresponds to a mixture of dyads, squares, and tight six-node configurations

(a square plus two adjacent nodes). The lower γ plateau favors the six-node configuration in terms of the cluster energies, but the larger features are even more difficult with which to tile the lattice than for squares.

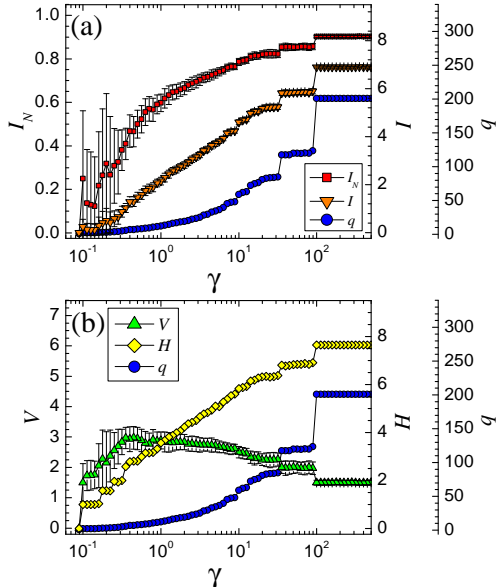


Fig. 34. The multiresolution analysis of a square lattice with periodic boundary conditions. Neighbors have an initial weight of $A_{ij} = 1$ and non-neighbors have an initial weight of $B_{ij} = 1$. We further apply a “potential” shift of $\phi_0 = 0.97995$ in order to be consistent with our previous analysis on glasses. There are three distinct plateaus in the information measures. A depiction of the system at $\gamma = 60$ for the center plateau is shown in Fig. 35.

0.2 Triangular lattice

Similar to the square lattice we define a uniform, initially unweighted, triangular lattice with $N = 400$ nodes. Edges are assigned to each triangular neighbor using periodic boundary conditions. The “potential” shift is $\phi_0 = 0.969925$. We again perform the same multiresolution analysis to the graph with the results shown in Fig. 36. There are three dominant plateaus in the information measures; and the overall multiresolution pattern resembles both the square lattice and the LJ systems except for the presence of the plateaus here.

We select a configuration at $\gamma = 50$ corresponding to the “left” plateau. The lattice is depicted in Fig. 37 with $q = 104$ clusters of 17 triads, and 86 “diamonds”, and 1 five-node cluster. The five node cluster is a result of a preference being given for an isolated node to join a diamond as opposed to forming its own single-node cluster. At this resolution, the diamond configuration dominates.

Two plateaus to the right of $\gamma \gtrsim 65$ are both strongly dominated by triads of nodes. The distinction between the two is that the central plateau favors an isolated node joining a triangle, to form a rare diamond, rather than

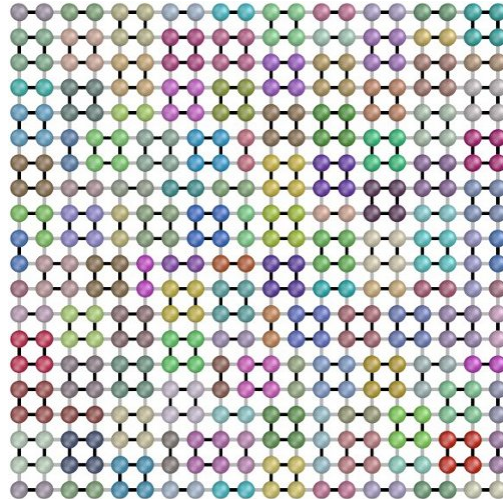


Fig. 35. A partition of a square lattice with periodic boundary conditions. The corresponding multiresolution plot is seen in Fig. 34. We use the algorithm described in the paper at $\gamma = 60$ to solve the system. To aid in visualization of the clusters, neighbor links *not in the same cluster* are made partially transparent. In this configuration, there were $q = 120$ clusters with 78 squares, 4 triads, and 38 dyads which indicates that square configuration dominates the partition, and it shows how our algorithm can naturally identify the basic unit cells of the square lattice.

forming its own single-node cluster. Together, the different plateaus show that our algorithm is able to isolate the basic unit cells of the lattice in a natural fashion.

0.3 Cubic lattice

We further define a uniform, initially unweighted, cubic lattice with $N = 1000$ nodes. Edges are assigned to each neighbor in the x , y , and z directions using periodic boundary conditions. The “potential” shift is $\phi_0 = 0.987988$. We perform the same multiresolution analysis to the graph as in the previous systems where the results are summarized in Figs. 38 and 39.

Out of $q = 177$ clusters, we identified 66 squares, 51 six-node configurations (square plus two adjacent nodes), 45 cubes, and 15 other assorted configurations smaller than cubes. At $\gamma \simeq 50$, the cube is the preferred cluster in terms of the cluster energy, but they consist of only slightly more than 25% of the clusters because the large cube configuration is more difficult to identify due to the perfect network symmetry and local constraints imposed by the evolution of the community structure during the algorithm dynamics. The “middle” plateau represents a square-dominated region (201 out of 294 clusters are squares), and the “right” plateau consists of dyads of neighbor nodes almost exclusively.

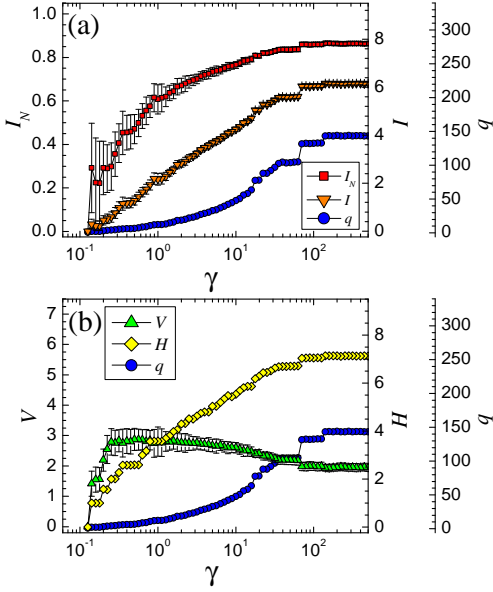


Fig. 36. The multiresolution analysis of a triangular lattice with periodic boundary conditions. Neighbors have an initial weight of $A_{ij} = 1$ and non-neighbors have an initial weight of $B_{ij} = 1$. We further apply a “potential” shift of $\phi_0 = 0.969925$ in order to be consistent with our previous analysis on glasses. There are three distinct plateaus in the information measures, but the latter two are closely related (see text). A depiction of the system at $\gamma = 50$ for the left plateau is shown in Fig. 37.

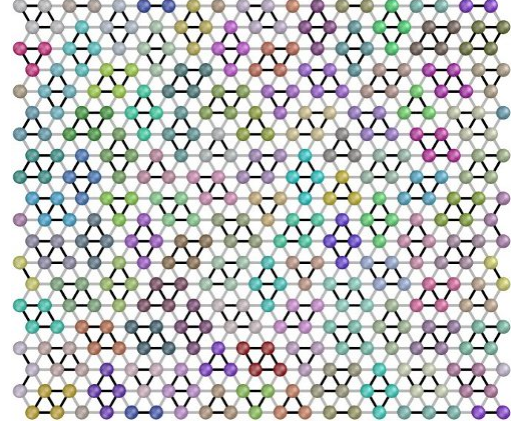


Fig. 37. A partition of a triangular lattice with periodic boundary conditions. The corresponding multiresolution plot is seen in Fig. 36. We use the algorithm described in the paper at $\gamma = 50$ (the “left” plateau) to solve the system. To aid in visualization of the clusters, neighbor links *not in the same cluster* are made partially transparent. In this configuration, there were $q = 104$ clusters with 17 triads, 86 “diamonds,” and 1 five-node configuration (see text) which indicates that the diamond configuration dominates the partition. Our algorithm can naturally identify the different basic unit cells of the lattice. By varying ϕ_0 (and the corresponding γ) we detect natural structures on varying scales.

P Multiresolution application to a 2D Ising lattice

We define two-dimensional square lattice of Ising spins using the Hamiltonian

$$H = - \sum_{ij} \sigma_i \sigma_j \quad (11)$$

for all pairs of neighbor spins i and j . Neighbors with the same spin have an initial weight of $A_{ij} = 1$, neighbors with opposite spins have an initial weight of $B_{ij} = 1$, and non-neighbors have an initial weight of $B_{ij} = 0$. There is an unavoidable inherent discontinuity in defining the interactions for the Ising system (only *neighbors* can interact) and the continuous systems elsewhere in this paper (*all* pairs of nodes interact). With this caveat, we analyze this Ising system according to the same multiresolution analysis, and we then compare the results to the other tested systems. We apply $s = 8$ replicas and $t = 8$ trials.

We could effectively treat the above Ising interactions using an *unweighted* network model since we can factor out the weight, but we again wish to maintain a consistent analysis across all systems in this paper. With this in mind, we further apply the average “potential” shift ϕ_0 which varies on each defined network and which corresponds to the negative of the average weight over *all* pairs of nodes (including non-neighbors). We allow zero energy moves for the solution dynamics. No overlapping nodes are assigned in the lattice.

In Fig. 40, there are two main plateaus for $\gamma \gtrsim 100$ and a noticeable configuration “shift” at $\gamma \simeq 100$. The “right” plateau for $\gamma \gtrsim 500$ consists largely of same-spin dyads except where a given spin has no matching neighbors. The “middle” plateau for $100 \lesssim \gamma \lesssim 500$ corresponds to a “natural” grouping of medium size clusters. In Fig. 41, different colors represent distinct clusters (best viewed in color) and edges *between* clusters (neighbor spins with the *same sign* but that are in *different* clusters) are depicted in gray. Missing edges are not shown

Here, the plateaus correspond to a cascade of structures starting from the smallest dyads of nodes, to basic plaquette structures (square, triangle, etc.), and growing ever larger (two joined plaquettes etc.). In Ising spin systems at different temperatures on a square lattice, the domains of “+” and “−” spins are physically separated from one another by domain walls. The plateaus here similarly correspond to the cascade of small plaquettes found on the lattice up to a cutoff scale set by the domain walls.

The domain walls are closely related to the *maximum* in VI (NMI displays a different, non-extremal, behavior where the standard deviation is large). Physically, they correspond to the scales at which the largest fluctuations occur where the large fluctuations result in poor information correlations between the replicas. Fig. 42 shows a sample depiction of the system at this VI peak. Correlation lengths are thus likely related to poorly correlated replicas best indicated by a VI *maximum*.

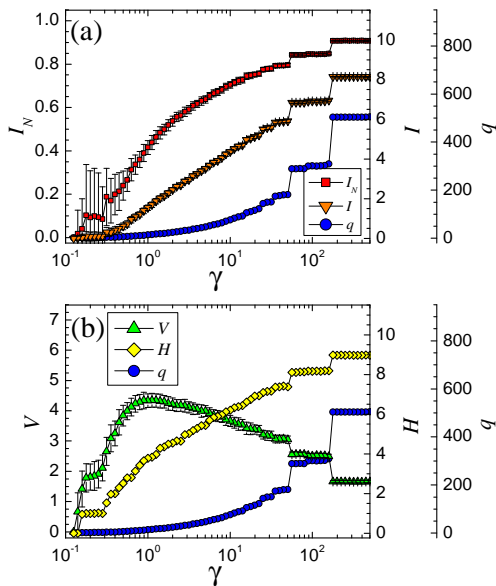


Fig. 38. The multiresolution analysis of a cubic lattice with periodic boundary conditions. Neighbors have an initial weight of $A_{ij} = 1$ and non-neighbors have an initial weight of $B_{ij} = 1$. We further apply a “potential” shift of $\phi_0 = 0.987988$ in order to be consistent with our previous analysis on glasses. There are three distinct plateaus in the information measures. The leftmost short plateau is the cube preferred resolution (in terms of cluster energy) with 45 out of 177 clusters are cubic clusters (no configurations larger than cubes are found). A depiction of the system at $\gamma = 50$ for the left plateau is shown in Fig. 39.

Q Multiresolution analysis of Lennard-Jones systems with elastic defects

We define a uniform lattice based on a two-dimensional Lennard-Jones system using the LJ potential in Eq. (2) where the lattice is constructed as the ideal ground state of the system using periodic boundary conditions. The main purpose is to check for consistency of our multiresolution method, but the lattice also allows us to perform a preliminary investigation of the behavior of our analysis in how it places lattice defects that are randomly inserted into the system. We used $s = 8$ replicas and $t = 8$ trials.

The ground state of the LJ system is given by a triangular lattice with a lattice constant that is equal to the distance that minimizes the LJ interaction between two atoms. We define a uniform triangular lattice with $N = 2943$ nodes where we create random “defects” by removing some nodes. Edges are again assigned and weighted according to the LJ potential in Eq. (2) applying periodic boundary conditions. (The “potential” shift is, as before, set to $\phi_0 = 0.969925$.) We perform the multiresolution analysis on the graph where the results are shown in Fig. 43.

Next, we select a configuration at $\gamma \simeq 31.6$ from the peak corresponding to the largest natural communities for this system at this specific lattice spacing. An example of the best lattice partition is depicted in Fig. 44. Defects ap-

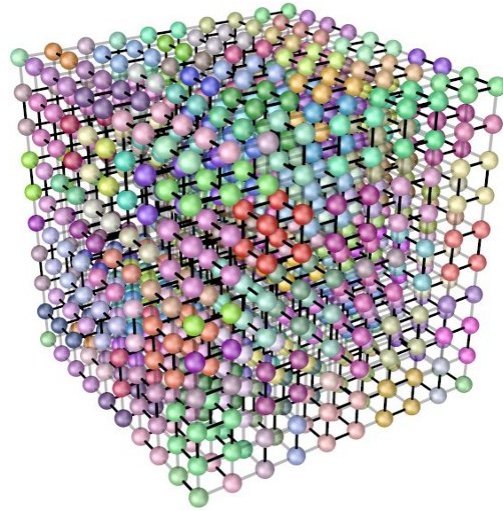


Fig. 39. A partition of a cubic lattice with periodic boundary conditions. The corresponding multiresolution plot is seen in Fig. 38. We use the algorithm described in the paper at $\gamma = 50$ (the short “left” plateau) to solve the system. To aid in visualization of the clusters, neighbor links *not in the same cluster* are made partially transparent. In this configuration, there were $q = 177$ clusters with 66 squares, 51 six-node configurations, 45 cubes, and 15 other assorted configurations. The cubic cluster is the preferred partition (in terms of cluster energy), but it is difficult to fill the system with cubes in practice due to the perfect symmetry of the network.

pear to occur most likely *near the boundary of neighboring communities*.

R Multiresolution analysis in space-time

In addition to the potential interaction energies, we may model our multiresolution community detection analysis using the mechanical action

$$S = \frac{1}{2} \int dt \left[\sum_{i=1}^N M_i \left(\frac{d\mathbf{r}_i}{dt} \right)^2 - \frac{1}{2} \sum_{i \neq j} \phi(\mathbf{r}_i, \mathbf{r}_j) \right]. \quad (12)$$

Here, M_i is the mass of particle i and $\mathbf{r}_i(t)$ denotes its location as a function of time. As throughout, ϕ is the two particle interaction. Below, we refer to the case of a system in D spatial dimensions. In a discretized form (allowing, in particular, for discrete time steps Δt along the time axis), the action

$$S = \sum_{\alpha\beta} W_{\alpha\beta} \quad (13)$$

with the nodes α and β representing nodes in space-time and $W_{\alpha\beta}$ an effective “interaction weight” between them. Thus, we represent our physical system as a network embedded in $(D + 1)$ dimensional space-time. We extremize this action “ S ” corresponding to the Hamiltonian of Eq. (3). The spatial links are determined by $\phi(\mathbf{r}_i, \mathbf{r}_j)$ similar to before (apart from a sign inversion) while the links

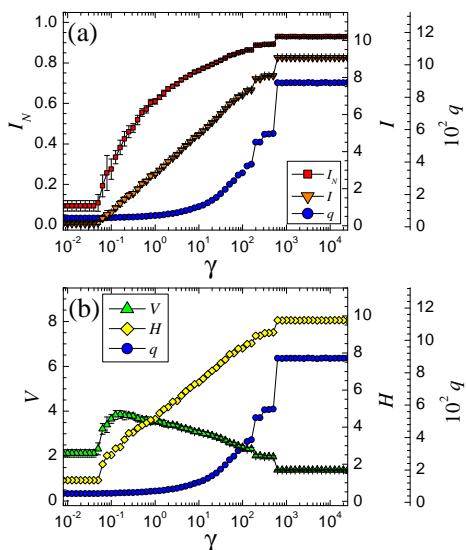


Fig. 40. A plot for the multiresolution analysis of a square lattice of Ising spins with periodic boundary conditions at a simulation temperature of $T = 2.269$ (close to the transition temperature). Neighbors with the same spin have an initial weight of $A_{ij} = 1$, neighbors with opposite spins have an initial weight of $B_{ij} = 1$, and non-neighbors have an initial weight of $B_{ij} = 0$. There are two distinct plateaus in the information measures for $\gamma \gtrsim 100$ with a significant configuration shift near $\gamma \simeq 100$. A depiction of the system at $\gamma = 400$ for the center plateau is shown in Fig. 41.

parallel to the time axis are determined by the particle masses. As before, extrema of the information theory correlation pinpoint the natural structures and scales in the system. In this case, there is only one tuning parameter γ as applied to different replicas of complete space-time networks. Thus, the space and time scales cannot be independently adjusted and are intertwined and are related by a ratio which is the typical speed of sound c (or an appropriate average of such speeds) in equilibrated solids.

S Continuum elasticity about local minima and the shear penetration depth

The focus of our article is on a detailed bona fide description of amorphous materials that invokes graph theory methods to ascertain general structure. The various examples shown have hopefully clearly outlined the strengths of our approach. In this section, we depart from this approach and outline a continuum formalism.

Continuum elasticity in regular solids does not assume detailed knowledge of the underlying atomic constituents. In this section, we follow suit and outline general considerations for amorphous solids. In an ideal crystalline system, any small deformation about the crystalline ground state will raise the energy in a harmonic manner. The increase of energy (for non-plastic deformations) is captured by

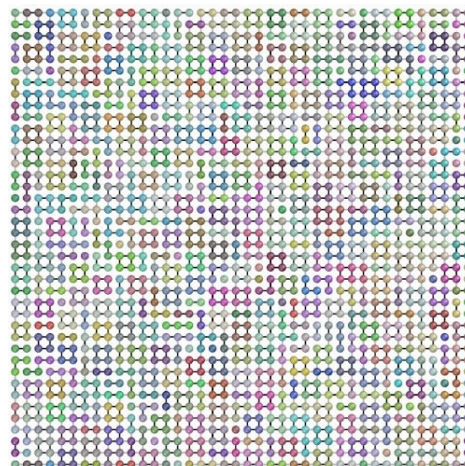


Fig. 41. A depiction of a partition of a square lattice of Ising spins with periodic boundary conditions at a simulation temperature of $T = 2.269$ (proximate to the critical temperature). The corresponding multiresolution plot is seen in Fig. 40. We use the algorithm described in the paper at $\gamma = 400$ (corresponding to the transition to the plateau with the highest NMI / lowest VI value) to solve the system. For presentation purposes, we depict all spins by spheres and links that cross a community boundary as grey edges. As with the multiresolution analysis of the square lattice, this multiresolution analysis shows that the dominant communities are square plaquettes within same-spin domains.

the elastic constants of the material. Nothing prevents, in principle, the application of these considerations for deformation about local energy minima – as these pertain to an amorphous solid in a local energy minimum (an *inherent* structure as it would have pertained to supercooled liquids). In what briefly follows, we consider the harmonic expansion of Eq. (12) about such a local energy minimum state. We then review general considerations about “shear penetration depth” - the length scale on which the medium reacts to shear. Earlier treatments considered the shear penetration depth in homogeneous media [111,112]. Here, we consider what may occur when replicating these considerations for deformations about a general non-uniform local ground state.

In what follows, we label the displacement of the i -th atom, \mathbf{u}_i about its position in a given state, \mathbf{R}_i by

$$\mathbf{u}_i = \mathbf{r}_i - \mathbf{R}_i. \quad (14)$$

In Eq. (14), \mathbf{r}_i denotes the location of the displaced atoms. Henceforth, we consider a coarse grained description in which \mathbf{u} is a field defined in the continuum. (That is, we replace the lattice indices i in Eq.(14) by continuous spatial coordinates x .) The displacement vector \mathbf{u} is a D -dimensional vector in real space. We apply field theoretic ideas introduced by [113]. In particular, we next follow the procedure of [30,111,112] and write the corresponding action of the system in a manner similar to that of the energy of an anisotropic solid in $(D + 1)$ dimensions. We will label the time direction as the $\alpha = 0$ direction and denote all spatial Cartesian coordinates by $\alpha = 1, 2, \dots, D$.

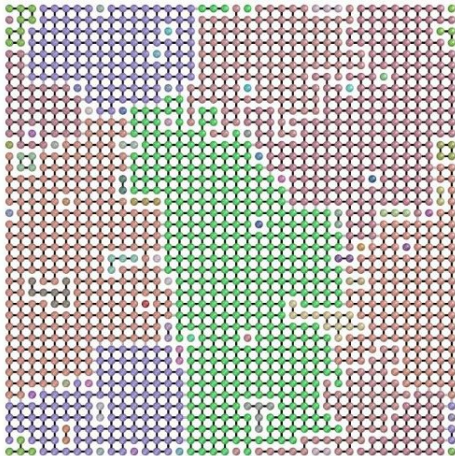


Fig. 42. A partition of a square lattice of Ising spins with periodic boundary conditions at a simulation temperature of $T = 2.269$. The corresponding multiresolution plot is seen in Fig. 40. We use the algorithm described in the paper at $\gamma = 3.60 \times 10^{-4}$, corresponding to the *peak* VI, to solve the system. For presentation purposes, we depict all spins by spheres and links that cross a community boundary as grey edges. The identified clusters vary substantially across the replicas (maximum fluctuations), but they are of the scale of the size of the spin domains. This qualitatively implies that the poor information correlations are naturally correlated with the individual domains of “+” and “-” spins. At this scale, the fluctuations are largest (and hence the related weakest information theory correlations). This scale on which fluctuations are maximal (coinciding with the Ising domain walls) should be contrasted with that of Fig. 41 for which the fluctuations were minimal (lowest variation of information (VI)) and the normalized mutual information (NMI) was the highest.

We will use Latin indices $a = 1, 2, \dots, D$ to label the spatial directions alone. In the continuum limit, expanding the energy to harmonic order about any local minima (inherent state), the action reads [111, 30],

$$S = \frac{1}{2} \int d^D x \int dt \partial^\alpha u^a C_{\alpha\beta ab}(x, t) \partial^\beta u^b. \quad (15)$$

In Eq. (15), repeated indices are to be summed over. The quantities $C_{\alpha\beta ab}$ derive from effective elastic moduli. In regular solids, $C_{\alpha\beta ab}$ are space (and time) independent quantities. In an amorphous medium, however, $C_{\alpha\beta ab}(x, t)$ are generally *space (and time) dependent*. The effective elastic constant C_{00ab} in Eq. (15) is set by the mass density, i.e., $C_{00ab} = \rho(x, t)$. [30, 111, 112] When α and β both assume values between 1 and D , the quantities $C_{\alpha\beta ab}$ are set by the elastic moduli of the solid (e.g., the shear modulus μ). The square root of the typical ratio between the usual spatial elastic moduli and those along the time axis for the space-time representation of the solid in Eq. (15) is given by a typical speed of sound in the system $c = \mathcal{O}(\sqrt{\mu/\rho})$.

One approach to defining defects such as dislocation and disclinations in regular solids is to consider the net change in the displacement or local orientation associated

with closed trajectories. Defect densities relative to a given inherent state may be defined in a similar way. More formally, we can dualize (via a Hubbard Stratonovich transformation) the quadratic action of Eq.(15) and associate the dual fields with defect current densities in space-time. Replicating the analysis performed for regular solids in [30, 111, 112] to amorphous solids with an invertible space-time dependent elastic moduli $C_{\alpha\beta ab}$, we obtain the same result obtained for regular solids. Namely, dislocation and disclination current densities are given by

$$\begin{aligned} J_{\alpha\beta}^a &= \epsilon_{\alpha\beta\lambda\rho} \partial^\lambda \partial^\rho u^a \\ T_{\gamma\delta}^{\alpha\beta} &= \epsilon_{\gamma\delta\lambda\rho} \partial^\lambda \partial^\rho \omega^{\alpha\beta}, \end{aligned} \quad (16)$$

with the local rotation given by

$$\omega_{\alpha\beta} = \frac{1}{2} \epsilon_{\alpha\beta\lambda a} \partial_\lambda u^a. \quad (17)$$

The temporal direction ($\alpha = 0$) components of these tensors are the usual (dislocation and disclination) defect densities of elasticity,

$$\begin{aligned} \alpha_i^a &= \epsilon_{ijk} \partial^j \partial^k u^a \\ \Theta_i^a &= \frac{1}{2} \epsilon_{ijk} \epsilon^{abc} \partial^j \partial^k \partial_b u^c. \end{aligned} \quad (18)$$

The condition of a divergence-less stress tensor (σ) in the absence of an applied force, enables us to write it as a curl of a gauge field,

$$\sigma_\alpha^a = \epsilon_{\alpha\beta\lambda} \partial^\beta B^{\lambda a}. \quad (19)$$

Elastic shear is mediated by the gauge field B . When a plastic component of the displacement field \mathbf{u} exists, it couples minimally to the stress-gauge fields via

$$S_{dist} = \int d^D x dt B^{\alpha a} J_{\alpha a} \quad (20)$$

for the coupling between the dislocation currents and gauges. Mathematically, the structure is very similar to that in electromagnetism when currents couples minimally to gauge fields. Just as charges screen applied electromagnetic fields (as, e.g., in the Debye screening of plasmas), defect charges can screen the elastic shear. In the uniform medium, when a defect condensate ($|\Psi_0| \neq 0$) appears, it gives rise a screening of the elastic shear [30, 111], with a screening length set by

$$\lambda_{shear} = \frac{c_T}{|\psi_0| \sqrt{\mu}}. \quad (21)$$

In Eq. (21), c_T is the transverse sound velocity and μ is the shear modulus. In the case of simple dilation of the elastic moduli when $C_{\alpha\beta ab}(x, t) = w(x, t) K_{\alpha\beta ab}$ where $K_{\alpha\beta}$ is a space-time independent tensor and w is a dilation function, the calculation of the elastic shear penetration depth can be replicated for the amorphous system to yield Eq. (21) when the quantities refer to the local values of λ_{shear} , c_T , ψ_0 , and μ . A similar effect appears for general

space-time dependent elastic moduli [114] when considering elastic deformations about a local energy minimum. As is seen from Eq. (21), *when the defect density tends to zero, the elastic shear penetration depth diverges*

$$\lambda_{shear} \rightarrow \infty \quad (22)$$

as the system becomes rigid throughout. In order to ascertain detailed shear response in a system, we may employ the shear stress correlation functions as link weights within our community detection algorithm. This is topic of a future study.

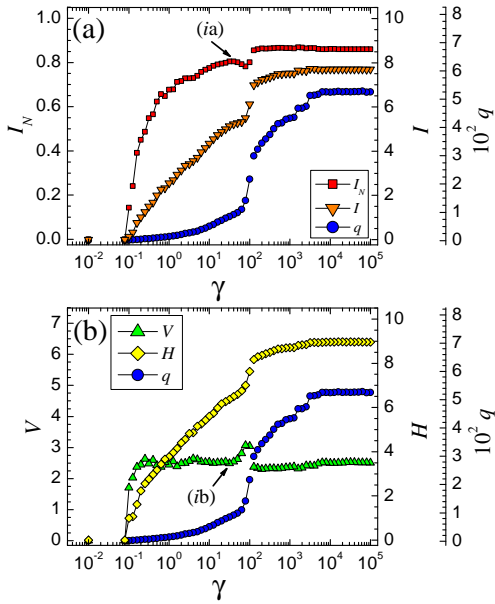


Fig. 43. A multiresolution analysis of a 2D triangular LJ lattice with periodic boundary conditions. Edges are weighted according to the LJ potential in Eq. (2) (with a potential shift $\phi_0 = 0.969925$). There are two preferred regions: a small peak on the left and a large plateau on the right, where the peak here corresponds to the largest possible “natural” clusters. The defects make only a small alteration to the multiresolution plot. A depiction of the system at $\gamma \simeq 31.6$ for the left peak is shown in Fig. 44.

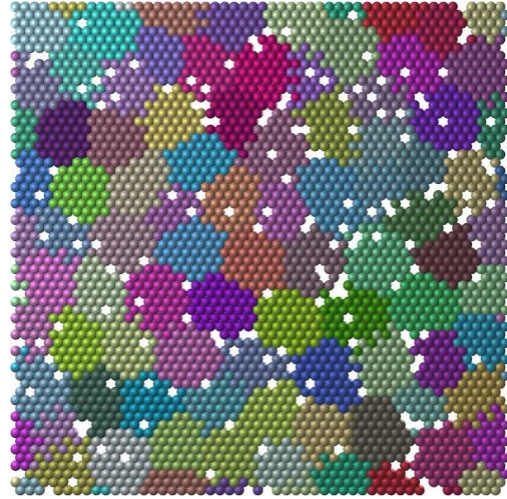


Fig. 44. A depiction of a partition of a 2D LJ triangular lattice with periodic boundary conditions. The corresponding multiresolution plot is seen in Fig. 43. We use the algorithm described in the paper at $\gamma \simeq 31.6$ (the left peak) to solve the system. Our algorithm places defects generally near the boundary of the communities in order to minimize the energy cost of the defects in the community assignments.

References

1. P. Ronhovde, S. Chakrabarty, M. Sahu, K. K. Sahu, K. F. Kelton, N. Mauro, and Z. Nussinov, <http://arxiv.org/pdf/1101.0008> (2010).
2. R. Zallen, *The Physics of Amorphous Solids*, John Wiley & Sons, Inc., pages 23–32 (1983).
3. A. L. Greer and E. Ma, *MRS Bulletin* **32**, 611 (2007).
4. B. C. Hancock and M. Parks, *Pharmaceutical Research* **17**, 397 (2000).
5. M. Telford, *Materials Today* **7**, 36 (2004).
6. M. Wuttig, and N. Yamada, *Nature Materials* **6**, 824 (2007).
7. J. Zaanen, *Nature* **404**, 714 (2000).
8. S.A. Kivelson, I. P. Bindloss, E. Fradkin, V. Oganesyan. J. M. Tranquada, A. Kapitulnik, and C. Howald, *Rev. Mod. Phys.* **75**, 1201 (2003).
9. T. Schenk, D. Holland-Moritz, V. Simonet, R. Bellissent, and D. M. Herlach, *Phys. Rev. Lett.* **89**, 075507 (2002).
10. K. F. Kelton, G. W. Lee, A. K. Gangopadhyay, R. W. Hyers, T. J. Rathz, J. R. Rogers, M. B. Robinson and D. S. Robinson, *Phys. Rev. Lett.* **90**, 195504 (2003).
11. D. R. Nelson, “Defects and Geometry in Condensed Matter Physics”, Cambridge University Press, Cambridge (2002).
12. J. F. Sadoc and R. Mosseri, “Geometrical Frustration”, Cambridge University Press, Cambridge (1999).
13. G. Tarjus, S. A. Kivelson, Z. Nussinov, and P. Viot, *J. Phys.: Condens. Matter* **17**, R1143 (2005).
14. Z. Nussinov, *Phys. Rev. B* **69**, 014208 (2004).
15. V. Lubchenko and P. G. Wolynes, *Annu. Rev. Phys. Chem.* **58**, 235 (2007).
16. L. Angelani, G. Parisi, G. Ruocco, and G. Vilianni, *Phys. Rev. E* **61**, 1681 (2000).
17. G. Parisi, *Physica A* **280**, 115 (2000).
18. S. Sastry, P. G. Debenedetti, and F. H. Stillinger, *Nature* **393**, 554 (1998).
19. P. G. Debenedetti and F. H. Stillinger, *Nature* **410**, 259 (2001).
20. V. Lurchenko and P. G. Wolynes, *J. Chem. Phys.* **121**, 2852 (2004).
21. W. L. Johnson, M. D. Demetriou, J. S. Harmon, M. L. Lind, and K. Samwer *MRS Bulletin* **32**, 644 (2007).
22. Jonathan P. K. Doye, David J. Wales, Fredrik H. M. Zetterling, and Mikhail Dzugutov, *J. Chem. Phys.* **118**, 2792 (2008).
23. T.R. Kirkpatrick, D. Thirumalai, and P. G. Wolynes, *Physical Review A* **40**, 1045 (1989).
24. M. Tarzia and M. A. Moore, *Physical Review E* **75**, 031502 (2007).
25. W. Gotze, *J. Phys.: Condes. Matter* **11**, A1 (1999).
26. P. Mayer, K. Miyazaki, and D.R. Reichman, *Phys. Rev. Lett.* **97**, 095702 (2006).
27. J. P. Garrahan, *J. Phys.: Condens. Matter* **14**, 1571 (2002).
28. D. Kivelson, S. A. Kivelson, X. Zhao, Z. Nussinov, and G. Tarjus, *Physica A* **219**, 27 (1995).
29. F. Ritort and P. Sollich, *Adv. Phys.* **52**, 219 (2003).
30. V. Cvetkovic, Z. Nussinov, and J. Zaanen, *Philos. Mag.* **86**, 2995 (2006).
31. E. Aharonov, E. Bouchbinder, H. G. E. Hentschel, V. Ilyin, N. Makedonska, I. Procaccia, and N. Schupper, *Euro. Phys. Lett.* **77**, 56002 (2007).
32. L. Berthier and G. Biroli, [arXiv: 1011.2578](https://arxiv.org/abs/1011.2578) (2010).
33. D. Chandler and J. P. Garrahan, *Ann. Rev. Phys. Chem.* **61**, 191 (2010).
34. A. Montanari and G. Semerjian, *Journal of Statistical Physics* **125**, 23-54 (2006).
35. H. Tanaka, T. Kawasaki, H. Shintani, and K. Watanabe, *Nature Materials* **9**, 324 (2010).
36. M. Mosayebi, E. D. Gado, P. Iig, and H. C. Ottinger, *Phys. Rev. Lett.* **104**, 205704 (2010).
37. L. Berthier, G. Biroli, J.-P. Bouchaud, L. Cipelletti, D. El Masri, D. L’Hote, F. Ladieu, and M. Pierno, *Science* **310**, 1797 (2005).
38. S. Karmakar, C. Dasgupta, and S. Sastry, *Proc. Natl. Acad. Sci. U.S.A.* **106**, 3675 (2010).
39. G. Biroli, J.-P. Bouchaud, A. Cavagna, T. S. Grigera, and P. Verrocchio, *Nature Physics* **4**, 771 (2008).
40. G. Biroli and J. -P. Bouchaud, e-print [arXiv:0912.2542](https://arxiv.org/abs/0912.2542) (2009).
41. J. Kurchan and D. Levine, e-print [arXiv:0904.4850](https://arxiv.org/abs/0904.4850) (2009).
42. J. D. Bernal, *Nature* **185**, 68 (1960).
43. D. B. Miracle, W. S. Sanders, and O. N. Senkov, *Philos. Mag.* **83**, 2409 (2003).
44. D. B. Miracle, *Nature Materials* **3**, 697-702 (2004).
45. D. B. Miracle, T. Egami, M. K. Flores, and K. F. Kelton, *MRS Bulletin* **32**, 629 (2007).
46. D. B. Miracle, E. A. Lord, and S. Ranganathan, *Materials Transactions* **47**, 1737 (2006).
47. W. K. Luo, H. W. Sheng, F. M. Alamgir, J. M. Bai, J. H. He, and E. Ma, *Phys. Rev. Lett.* **92**, 145502 (2004).
48. P. Ganesh and M. Widom, *Phys. Rev. B* **77**, 0145205 (2008).
49. Y. T. Shen, T. H. Kim, A. K. Gangopadhyay, and K. F. Kelton, *Phys. Rev. Lett.* **102**, 057801 (2009).
50. E. D. Gado, P. Iig, M. Kroger, and H. C. Ottinger, *Phys. Rev. Lett.* **101**, 095501 (2008).
51. W. Kob, C. Donati, S. J. Plimpton, P. H. Poole, and S. C. Glotzer, *Phys. Rev. Lett.* **79**, 2827 (1997).
52. E. R. Weeks, J. C. Crocker, A. C. Levitt, A. Schofield, and D. A. Weitz, *Science* **287**, 627 (2000).
53. A. Widom-Cooper, P. Harrowell, and H. Fynewever, *Phys. Rev. Lett.* **93**, 135701 (2004).
54. J. D. Stevenson, J. Schmalian, and P. G. Wolynes, *Nature Physics* **2**, 268 (2006).
55. L. Berthier, G. Biroli, J.-P. Bouchaud, and R. L. Jack, e-print:1009.4665 (2010).
56. H. W. Sheng, W. K. Luo, F. M. Alamgir, J. M. Bai, and E. Ma, *Nature* **439**, 419 (2006).
57. J. L. Finney, *Proc. R. Soc. London, Ser. A* **319**, 479 (1970).
58. J. Dana Honeycutt and Hans C. Andersen, *J. Phys. Chem.* **91**, 4950 (1987).
59. P. J. Steinhardt, D. R. Nelson and M. Ronchetti, *Phys. Rev. B* **28**, 784 (1983).
60. T. C. Hufnagel and S. Brennan, *Phys. Rev. B* **67**, 014203 (2003).
61. M. M. J. Treacy, J. M. Gibson, L. Fan, D. J. Paterson, and I. McNulty, *Rep. Prog. Phys.* **68**, 2899 (2005).
62. P. Ronhovde and Z. Nussinov, *Phys. Rev. E* **80**, 016109 (2009).
63. Peter Ronhovde and Zohar Nussinov, *Physical Review E* **81**, 046114 (2010).
64. M. Girvan and M. E. J. Newman, *Proc. Natl. Acad. Sci. USA* **99**, 7821 (2002).
65. S Fortunato, *Physics Reports* **486**, 75 (2010).

66. A. Lancichinetti and S. Fortunato, *Phys. Rev. E* **80**, 056117 (2009).
67. M. E. J. Newman and M. Girvan, *Phys. Rev. E* **69**, 026113 (2004).
68. V. D. Blondel, J.-L. Guillaume, R. Lambiotte, and E. Lefebvre, *J. Stat. Mech.* **10**, P10008 (2008).
69. M. E. J. Newman, *Phys. Rev. E* **69**, 066133 (2004).
70. J. Reichardt and S. Bornholdt, *Phys. Rev. E* **74**, 016110 (2006).
71. M. E. J. Newman, *Phys. Rev. E* **74**, 036104 (2006).
72. V. Gudkov, V. Montelaegre, S. Nussinov, and Z. Nussinov, *Phys. Rev. E* **78**, 016113 (2008).
73. A. Arenas, A. Daz-Guilera, and C. J. Perez-Vicente, *Phys. Rev. Lett.* **96**, 114102 (2006).
74. M. Rosvall and C. T. Bergstrom, *Proc. Natl. Aca. Sci. U.S.A.* **105**, 1118-1123 (2008).
75. Book chapter by U. Brandes, D. Dellng, M. Gaertler, R. Gorke, M. Hofer, Z. Nikoloski, and D. Wagner, "On finding graph clusterings with maximum modularity" in the book "Graph-theoretic concepts in computer science", Lecture notes in Computer Science, Springer Berlin/Heidelberg, DOI: 10.1007/978-3-540-74839-7 (2007).
76. M. Meila, *J. Multivariate Anal.* **98**, 873 (2007).
77. This includes, e.g., (i) relaxation processes of structural glass formers relating to slow global (α) process and local rapid rearrangements (β processes), and (ii) systems with multiple degrees of freedom (structural, magnetic, and other) that may exhibit transitions at different temperatures.
78. M. Mezard and A. Montanari, *J. Stat. Phys.* **124**, 1317 (2006).
79. S. Franz and A. Montanari, *J. Phys. A.* **40**, F251 (2007).
80. K. K. Sahu, N. A. Mauro, L. Longstreth-Spoor, D. Saha, Z. Nussinov, M. K. Miller, and K. F. Kelton, *Acta Materialia* **58**, 4199 (2010).
81. T. Egami, *J. Non-Cryst. Solids* **317**, 30 (2003).
82. J. Stadler, R. Mikula, and H. R. Trebin, *Int. J. of Mod. Phys. C* **8**, 1131 (1997).
83. M. Mihalkovič, C. L. Henley, M. Widom, and P. Ganesh, e-print arXiv:cond-mat.mtrl-sci/0802.2926 (2008).
84. VASP website: <http://cms.mpi.univie.ac.at/vasp/>
85. J. A. Moriarty and M. Widom, *Phys. Rev. B* **56**, 7905 (1997).
86. W. Kob and H. C. Andersen, *Phys. Rev. E* **51**, 4626 (1995).
87. L. C. Valdes, F. Affouard, M. Descamps, and J. Habasaki, *J. Chem. Phys.* **130**, 154505 (2009).
88. For overdamped systems (such as particles in viscous liquids) obeying "Aristotelian dynamics" ($\mathbf{F} \propto \mathbf{v}$), clusters in which the force on all their individual particles is nearly the same, will move with uniform velocity. This leads to a high inter-particle correlations between particles belonging to the same cluster.
89. D. Hu, P. Ronhovde, and Z. Nussinov, e-print arXiv:1008.2699 (2010).
90. A. Arenas, A. Fernandez, and S. Gomez, *New. J. Phys.* **10**, 053039 (2008).
91. J. M. Kumpula, J. Saramaki, K. Kaski, and J. Kertesz, *Fluct. Noise Lett.* **7**, L209 (2007).
92. A. Lancichinetti, S. Fortunato, and J. Kertesz, *New J. Phys.* **11**, 033015 (2009).
93. P. J. Mucha, T. Richardson, K. Macon, M. A. Porter, and J. -P. Onnella, *Science* **328**, 876 (2010).
94. D. J. Fenn, M. A. Porter, M. McDonald, S. Williams, and N. F. Johnson, *Chaos* **19**, 033119 (2009).
95. Asaph Widmer-Cooper, Heidi Perry, Peter Harrowell, and David R. Reichman, *Nature Physics* **4**, 711 (2008).
96. J. X. Lin, C. Reichhardt, Z. Nussinov, L. P. Pryadko, and C. J. Olson Reichhardt, *Physical Review E* **73**, 061401 (2006).
97. M. Lisa Manning and Andrea J. Liu, arXiv:1012.0064 (2010).
98. W. Donath and A. Hoffman, *IBM Journal of Research and Development* **17(5)**, 420 (1973).
99. M. Fiedler, *Czech. Math. J.* **23(98)**, 298 (1973).
100. Y. Kuramoto, *Chemical Oscillations, Waves and Turbulence* (Springer-Verlag, Berlin, Germany) (1984).
101. R. B. Griffiths, *Phys. Rev. Lett.* **23**, 17 (1969).
102. S. Chakrabarty, M. Widom, M. Mihalkovič, K. F. Kelton, and Z. Nussinov, in preparation
103. T. Nakamura, E. Matsubara, M. Sakurai, M. Kasai, A. Inoue, and Y. Waseda, *J. Non-Cryst. Solids* **312-314**, 517 (2002).
104. J. Saida, K. Itoh, K. Sato, M. Imafuku, T. Sanada, and A. Inoue, *J. Phys.:Cond. Matt.* **21**, 375104 (2009).
105. D. J. Sordelet, R. T. Ott, M. Z. Li, S. Y. Wang, M. F. Besser, A. C. Y. Liu, and M. J. Kramer, *Metallurgical and Materials Transactions A* **39**, 1908 (2007).
106. S. Y. Wang, C. Z. Wang, M. Z. Li, L. Huang, R. T. Ott, M. J. Kramer, D. J. Sordelet, and K. M. Ho, *Phys. Rev. B* **78**, 184204 (2008).
107. N. A. Mauro and K. F. Kelton, submitted to *Phys. Rev. B*.
108. R. L. McGreevy, *J. Phys.: Condens. Matter* **3** F9 (1991).
109. D. A. Keen and R. L. McGreevy, *Nature* **344**, 423-5 (1990).
110. T. H. Kim and K. F. Kelton, *J. Chem. Phys.* **126**, 054513 (2007).
111. J. Zaanen, Z. Nussinov, and S. I. Mukhin, *Annals of Physics* **310**, 181 (2004).
112. V. Cvetkovic, Z. Nussinov, S. Mukhin, and J. Zaanen, *Europhys. Lett.* **81**, 27001 (2008)
113. H. Kleinert, "Gauge fields in condensed matter, vol. II: Stresses and defects, Differential Geometry, Crystal Defects", World Scientific, Singapore (1989)
114. V. Cvetkovic, M. Vasin, and Z. Nussinov, in preparation.